Identification of Myeloid Protein Kinase C – Epsilon as a Novel Atheroprotective Gene

Alexis T. Wells PhD[1], Michelle M. Shen BS[1], Redwan H. Binrouf BS[1], Anna E. D'Amico PhD[1], Ramon Bossardi Ramos PhD[2], Michelle R. Lennartz PhD[1]

[1]Department of Regenerative and Cancer Cell Biology, [2]Department of Molecular and Cellular Physiology, Albany Medical College, 47 New Scotland Avenue, Albany, New York, 12208-3479, USA

Address correspondence to: Michelle R. Lennartz or Alexis T. Wells, 47 New Scotland Ave, Room MS-309, Albany Medical College, Mail Code 165, Albany, New York 12208-3479, USA; Telephone: 518-262-5217; e-mail: LennarM@amc.edu or wellsa2@amc.edu

The authors have declared that no conflict of interest exists.

Background:

Atherosclerosis is a lipid mediated chronic inflammatory disease driven my macrophages (MØ). Protein Kinase C – epsilon (PKCε) is is a serine/threonine kinase involved in diverse cellular processes such as migration, growth, differentiation, and survival. PKCε is known to act in a context dependent manner within heart, however, its role in atherosclerosis is unknown.

Methods:

Bone marrow derived MØ from global PKCε KO mice were examined for impact of lipid metabolism and inflammatory factor secretion. Public geneset analysis assessed raw counts of PKCε to determine translational relevance. To determine the function myeloid PKCε on atherosclerosis a novel murine model was generated using LysM Cre technology. After its characterization, human-like hypercholesterolemia was induced to assess plaque morphology in WT mice or mice lacking myeloid PKCε.

Results:

Public geneset analysis of human atherosclerotic plaque tissue revealed that PKCε expression is inversely correlated with plaque size and vulnerability. Similarly, peritoneal MØ from hypercholesterolemic mice have significantly lower PKCε expression. As MØ play a major role in atherogenesis, we generated a mouse strain with PKCε selectively deleted in the myeloid lineage (mεKO). qPCR revealed no basal differences between genotypes in the expression of lipid uptake receptors, efflux transporters, or inflammatory markers. However, upon lipid loading, mεKO MØs retained significantly more cholesterol

than WT. Human-like hypercholesterolemia was induced in WT and mεKO mice and assessed for lesion area and plaque morphology in aortic arches and aortic roots. We found that, compared to WT, the lesion area in mεKO mice was significantly larger, more necrotic, had larger foam cells, and thinner collagen caps.

Conclusions:

Loss of myeloid PKCε promotes atherosclerosis as determined by larger lesions, more necrosis, thinner plaque caps). Together, these data identify myeloid PKCε as a novel atheroprotective gene, laying the foundation for mechanistic studies on the signaling networks responsible for the phenotype.

Graphical Abstract:

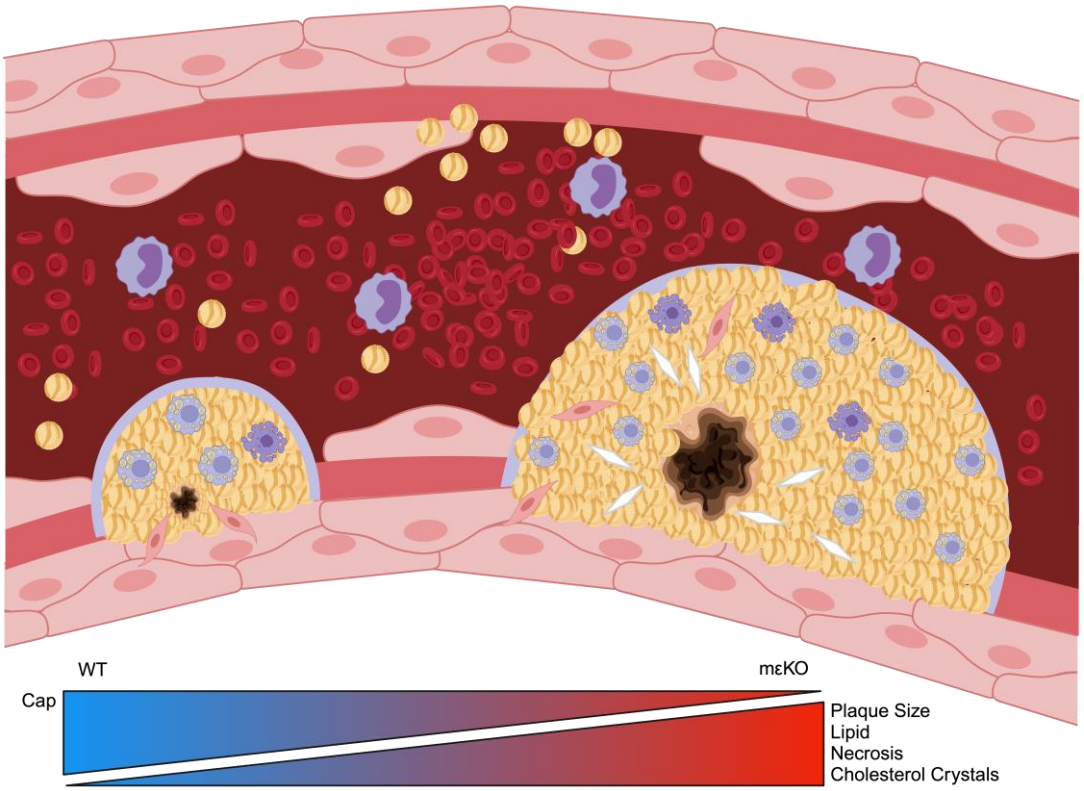

Created in BioRender. Wells, A. (2024) https://BioRender.com/ u28y100

Introduction

Cardiovascular disease (CVD) is the leading cause of death worldwide, with atherosclerosis being a major contributor (1, 2). Despite the widespread use of statins, CVD remains a major health care problem, accounting for 1 in 5 deaths in the U.S. (2022) and 12% of health care costs ($378 billion in 2017-2018) (3, 4). New strategies and targeted therapies are needed to combat these statistics, reducing atherosclerosis and the catastrophic effects (heart attack and stroke) of plaque rupture.

There is a cascade of events that occur during the development of atherosclerosis (Figure 2A) (5, 6). Macrophages (MØ) migrate to sites of endothelial damage, extravasate into the intima, and internalize modified and non-modified low-density lipoprotein (LDL) through scavenger receptors or LDLR. At later stages, cells within the plaque become apoptotic and, if not removed by efferocytosis, contribute to the necrosis prevalent in advanced plaques (7). While plaque size may vary, the more critical factor in assessing vulnerability is plaque composition (5, 6, 8). That is, human vulnerable plaques have thin fibrous caps, embedded collagen covered by new plaque growth, are foam cell rich, and have large necrotic cores (6, 8). This constellation of factors produces chronic inflammation that can result in thrombosis, leading to angina, myocardial infarction (MI), stroke, and even death (5, 9, 10).

Protein Kinase Cs are a family of master kinases, linked to virtually every known signaling network. Our previously published data suggests PKCε acts as an inflammatory signaling node (11). Its involvement in IgG-mediated phagocytosis, respiratory burst, and NF-κB activation has been well documented by ourselves and

others (4, 12-20). This suggests that PKCε moderates excessive inflammation; but *how* PKCε accomplishes this is a fundamental unanswered question.

PKCs act in protection and pathology, depending on context (16, 21-24). Active protein kinase C epsilon (PKCε) has been linked to inflammation in patients with atherosclerosis, hypertension-induced heart failure, and conversely, to protection against ischemia-reperfusion injury and myocardial infarction (21, 22, 24, 25). In the liver, PKCε influences cholesterol regulation by increasing the transcription of LDLR through extracellular signal-regulated kinase (ERK) and c-Jun N-terminal kinase (JNK) signaling pathways (26, 27). In vascular smooth muscle cells, PKCε inhibits apoptosis, increases MMP-2, -9 expression, and induces migration (26). As for cardiomyocytes, PKCε regulates the interaction between conexin43 and a potassium channel subunit (Kir6.1) within the mitochondria, preventing hypoxia-induced cell death (28). In MØ, PKCε has been linked to promoting aggregated LDL phagocytosis and resistin signaling via TLR4/MyD88, thus increasing lipid accumulation and inflammation (22, 26, 29, 30). In contrast, a large randomized clinical trial using high-dose adenosine (activator of PKCε) during acute MI found a significant *reduction* in infarct size (26, 31).

PKCε is perhaps best known as an oncogene, overexpressed in many cancers where it enhances tumor cell migration, invasion, and resistance to apoptosis (32-37). If applied to MØ and atherosclerosis, these properties could be atheroprotective. That is, PKCε may support MØ recruitment into early plaques, regulate the uptake/retention/efflux of cholesterol, promote cell survival extending MØ lifetime for increased efferocytosis, and protect against metrics of atherogenesis that contribute to MI and heart failure. Thus, the same PKCε processes that are pathological in cancer

may slow the development of atherosclerosis. However, the role of myeloid PKCε in atherosclerosis is unknown.

To study the impact of MØ PKCε in atherosclerosis, we generated LysMCre PKCε$^{fl/fl}$ (mεKO) mice, indiced hypercholesterolemia, and compared them to siblings lacking LysMCre (i.e., “wild type” with respect to PKCε expression). Using a variety of plaque metrics, we found that loss of myeloid PKCε produced plaques with a more advanced/more vulnerable phenotype. In vitro studies indicate that MØ foam cells have decreased PKCε expression, which parallels human data (PKCε is significantly lower in advanced plaques). Additionally, PKCε null MØ have increased lipid retention and secrete more TNFα, both pro-inflammatory responses. Taken together, this work presents multiple lines of evidence implicating MØ PKCε in athero-protection.

Methods

Sex as a biological variable/limitations of the study.

It is well known that atherosclerosis disproportionately affects human males vs pre-menopausal women (60). Thus, to maximize the chances of seeing phenotypic differences, this study was limited to males. It should be noted that males and females were included in the first cohort; the females did not remain hypercholesterolemic for the 16 weeks and did not produce plaques. The response of female mice to AAV8-PCSK9 strategy is reported to be lower than that of males, so the virus will have to be titrated (66) to ensure long-term hypercholesterolemia before determining the effect of MØ PKCε on female plaque progression.

Reagents.

ACK lysis buffer: 0.5 M NH_4Cl, 1 mM $KHCO_3$, and 0.1 mM EDTA (pH 7.4). Bone marrow media (BMM): DMEM containing 10% FBS, 20% L Cell media, 1% Na Pyruvate, 1% Glutamax, 0.03% sodium bicarbonate, 1% nonessential amino acids, and 50 μg/ml gentamicin. Cell media: BMM lacking L cell media. Sucrose lysis buffer/P3I: 50 mM Tris-HCl, pH 7.4, 0.25 M sucrose, 2.5 mM DTT, 2.5 mM EDTA, 5 mM benzamidine, 50 mg/mL leupeptin, 50 mg/mL aprotinin, 50 mg/mL trypsin inhibitor, 5 mg/mL pepstatin, 1 mM PMSF, 20 mM NaF, 1 mM Na_3VO_4, 1 mM para-nitro-phenylphosphate, 5 mM imidazole (Sigma). TBST: 5 mM Tris, pH 7.4 containing 150 mM NaCl and 0.1% Tween® 20.

Publicly available RNA-seq data.

Early and late human atheromas were analyzed using iDEP custom R code for differential expression.

Insoluble immune complexes.

10 µl of 10 mg/mL BSA (Sigma A0281) was added to 300 µl of 2 mg/mL rabbit anti-BSA IgG (Sigma, B1520) in Optimem™ buffer (ThermoFisher Scientific, 31985070). Complexes formed by rotation (1 h, 37°C). Complexes were pelleted and washed twice with Optimem, and resuspended to the initial volume. 15 µl of this stock solution was added/1 x 10^6 BMDM.

Global PKCε knockout mice (εKO).

PKCε$^{+/-}$ heterozygotes on the C57BL/6 background were purchased from Jackson Laboratory (*B6.129S4-Prkce^{tm1Msg}/J* stock# 004189; Bar Harbor, ME) and bred in the Albany Medical Center Animal Resources Facility. Global deletion of PKCε in mice leads to noticeably smaller offspring with an immunodeficiency causing εKO mice to succumb to infections and fall out of lineage. Heterozygotes were crossed to produce the wild-type and PKCε$^{-/-}$ (εKO) siblings. Cells from both male and female were used; there were no effects of sex or age (3-6 months) on experimental outcome. All animal procedures were approved by the Albany Medical Center Institutional Animal Care and Use Committee. Cells obtained from one mouse represent one independent experiment. All studies were conducted such that the experimenter was blinded to the genotype.

Myeloid selective PKCε knockout mouse (mεKO).

PKCε$^{fl/fl}$ mice were generated by IVF at Taconic Labs (Germantown, NY) from sperm provided by The Genome Editing and Animal Models Core at the University of Wisconsin (Madison) Biotechnology Center (71). This C57BL/6 congenic strain was deposited at The Jackson labs (B6(Cg)-*Prkce$^{tm1.1Akv}$*/LennMmjax stock# 69556). PKCε$^{fl/fl}$ animals were crossed with LysMCre (Jackson Laboratory, Strain #004781 B6.129P2-*Lyz2$^{tm1(cre)Ifo}$*/J) to produce LysMCre PKCε$^{fl/fl}$ hemizygotes. PKCε$^{fl/fl}$ females were crossed to LysMCre$^{+/-}$ PKCε$^{fl/fl}$ males to produce PKCε$^{fl/fl}$ offspring that lacked LysMCre (designated WT) and siblings expressing hemizygous LysMCre (**m**yeloid selective PKCε **k**nock**o**ut, designated mεKO). Compared to the parental C57BL/6 strain, there are no obvious size, behavioral, or health issues with either the WT or mεKO animals. All

animal procedures were approved by the Albany Medical Center Institutional Animal Care and Use Committee. Cells obtained from one mouse represent one independent experiment. All studies were conducted in a blinded fashion.

Elcited Peritoneal MØ (pMACs).

Mice were injected i.p. with 3 mL sterile 3% Thioglycolate solution. 4 days later, animals were euthanized and pMACs recovered by peritoneal lavage with 10mL PBS.

Bone marrow-derived MØ (BMDM).

Differentiated macrophages were derived from bone marrow stem cells as previously described (11). Briefly, mice were euthanized via isoflurane and cervical dislocation. Femurs and pelvises were removed and flushed for bone marrow collection. Red blood cells were lysed with ACK lysis buffer and the recovered stem cells were differentiated in BMM. BMDM were used 7-14 days after harvesting.

ELISA assays.

C57BL/6 and εKO BMDMs (1.5 x 10^6/well, 6 well plate) were incubated with or without immune complexes for 2h. Culture media was collected and IL6 and TNFα was quantified using BioLegend ELISA Max™ kits (431301 and 430901) per the manufacturer's instructions. Results are reported as as pg/mL net release.

Western blotting.

Brains were placed in sucrose lysis buffer/P3I and homogenized using a KINEMATICA Polytron PT 10 20 3500 115v. The homogenate was sonicated on ice 2 x 10 s (Sonics & Materials Vibra-cell VC High Intensity Ultrasonic Processor) and centrifuged (13,000 x g, 10 min 4°C) to remove particulates. 3 µg of protein (Bradford Assay) was used for western blots. *Spleens* were minced in PBS and passed through a 70 µm cell strainer (CELLTREAT, 229483). Erythrocytes were lysed with ACK buffer and splenocytes recovered by centrifugation (13,000 x g, 10 min 4°C). Splenocytes were solubilized in 400 µl sucrose lysis buffer, followed by sonication on ice (2 x 10 s). After clarification by centrifugation (13,000 x g, 10 min 4°C), protein was quantified (Bradford Assay); 100 µg was loaded/lane. BMDMs and pMACs were ACK lysed, resuspended in 100ul Sucrose Lysis Buffer, and sonicated for 7 seconds on ice. Samples were clarified by centrifugation (13,000 x g, 10 min 4°C), and protein was quantitated; 300 µg of protein/lane was used for western blots.

Proteins were separated on a 10% PAGE under reducing conditions. The Bio-Rad Precision Plus Protein Kaleidoscope ladder (1610375) served as the molecular weight standards. Gels were transferred onto a PVDF membrane using an iBlot® system. Membranes were blocked with 5% milk in TBST and washed 3 x TBST. Antibodies were diluted in 1% BSA/TBST (Table 1) and allowed to bind overnight (4°C with rocking); GAPDH was the loading control. The following day, membranes were washed 5 times with TBST, probed with goat α rabbit HRP secondary antibody (1:10,000 in 1% BSA/TBST) for 1 h RT while rocking. Membranes are then washed (5 times) and developed using Bio-Rad's Clarity Western ECL Substrate kit (1705060) according to the manufacturer's instructions. Membranes were imaged using a Bio-Rad

ChemiDoc™ MP Imaging System. Densitometry was used to quantify genotype differences in PKC expression. TIFF files were opened in FIJI and the Analyze → Gels function was used to generate peaks to the corresponding bands. Peaks were separated and the wand tool used to quantify the area of each band. For each band the background was subtracted, normalized to GAPDH and their WT counterparts. Fold change relative to C57BL/6 or WT was reported.

qPCR.

RNA from $1x10^6$ MØ were extracted with PureLink™ RNA Mini Kit (ThermoFisher Scientific, 12183018A); RNA purity and concentration was determined by Nanodrop. RNA was reversed transcribed using qScript cDNA SuperMix (QuantaBio, 95048-500). cDNA was then used for qPCR. Each 20 µl reaction contained 10 µl Quanta PerfeCTa Syber Green Fast Mix (QuantaBio, 95071-012), 8 nMol each forward and reverse primers, and 50 ng cDNA. Thermocycler Ct values were exported into an Excel file and the relative expression ($2^{-\Delta Ct}$) was calculated and reported. All samples were normalized to β-actin.

Global PKCε knockout lipid droplet formation and staining.

50,000 differentiated C57BL/6 and εKO BMDM were plated on coverslips in 24 well plates. Acetylated LDL (Kalen BioMedical, 770201-6; 360 µg/mL in BMM) was added. After 4 h, the cells were washed with PBS and fixed (4% PFA, 15 min, RT). Coverslips were washed with PBS, stained with BODIPY (ThermoFisher Scientific, D3922, 30 min)

and mounted. Z stacks were collected, 3-D reconstitutions were made, and droplet number and area was quantified using Imaris® software.

mεKO lipid uptake and retention.

42,000 WT and mεKO BMDM per well, with 4 technical replicates (48-well plate) was incubated with 50 μg/mL human highly-oxidized-LDL (Kalen Biomedical, #770252) in BMM for 24 h. Spent media was removed, and cells were washed 3 times with PBS and held at -80°C. Total and free cholesterol quantified using the Cholesterol Ester-Glow™ kit (Promega, J3190) according to the manufacturer's instructions. Technical replicates were averaged, and the difference between total and free cholesterol represents the cholesterol ester content.

Generation of hypercholesterolemic mice.

Cohort animals were identified and their eartags recorded. This code was not broken until all the data had been analyzed, thus blinding experimenters to animal genotype. Weights of 8-week-old mice were recorded at the time of retro-orbital injections of AAV8-PCSK9 ($1x10^{12}$ gc/200 μl sterile PBS). Animals were given a high fat (HFD, "Western") diet (TD.88137; Inotiv) for 16 weeks. At two weeks post-injection/HFD blood was collected (submandibular bleed) for plasma cholesterol measurements (Fujifilm Healthcare Americas Corp Cholesterol E kit, NC9138103); ≥500 mg/dL was considered hypercholesterolemic. In rare cases, if 2-week plasma cholesterol did not reach 500 mg/dL, a second AAV8 injection was done and cholesterol measurements done two weeks later. The final experimental conditions were chosen from the results of a pilot

experiment. Pilot experiments: 16 mice (8 male, 8 female; two timepoints 9- and 16-weeks post AAV8/HFD). Females had high plasma cholesterol at 2 weeks that decreased over time. Males remained hypercholesterolemic for the duration. At 9 weeks, no animals had visible plaque. At 16 weeks, males, but not females, had developed plaques. The lack of plaques in females correlates with their lack of sustained hypercholesterolemia. Thus, subsequent cohorts were male only, harvesting tissue 16 weeks after AAV8/HFD.

Tissue collection and processing.

Studies were terminated by isoflurane euthanasia and cervical dislocation. Blood was collected from the portal vein for plasma cholesterol determination. Animals were exsanguinated with 10 mL warm PBS through the left ventricle using a syringe and 25-gauge needle. Hearts and aortic arches/descending aortas were collected. The aortic arches were fixed (4% PFA overnight, RT) and stored at 4°C in PBS/Thimerosal. Hearts were cut in half perpendicular to the aorta; the upper half containing the aortic root, was cast into a cryomold using OCT and held at -80°C until sectioning. A total of 25 charged slides with 3-4 10 μm thick sections per slide were collected from each mouse so that each slide contained the beginning, middle, and end of the aortic root as previously described (67). Brifely, sequential sections were put on each slide, such that sections 1 to 25 went on slides 1 to 25. Sections 26 to 50 were placed on slides 1 to 25, respectively, and so on. This generated 25 slides containing multiple sections separated by 250 μm and spanning the entire plaque length. Thus, 1 slide obtained information along the entire plaque length.

Aortic arches.

En face preparations were conducted by opening the lumen, pinning the tissue flat, and staining with 0.3% ORO. Tissue area was defined by the aortic arch and 3 mm of the descending aorta (no plaque was present beyond 3 mm). Plaque area was quantitated in FIJI using the color thresholding macro and normalized to tissue area.

H&E staining and analysis.

Six sections spaced 40 μm away from one another per mouse was collected. Fresh tissue sections were fixed for 3 minutes in a solution comprised of 100% EtOH, 40% PFA, 100% Glacial acetic acid, and diluted with diH_2O to make a 4% PFA solution. Fixed sections were then dehydrated in 70% EtOH followed by 95% EtOH for 1 minute each. Tissues were then washed in running tap H_2O and diH_2O for 30 seconds each. Tissue was then stained with Hematoxylin for 4 minutes and washed with tap H_2O until clear. Stained samples were then clarified for 15 seconds, washed with tap H_2O, placed in bluing agent for 1 minute and then washed with tap H_2O. After Hematoxylin staining, tissues were placed in 95% EtOH followed by Eosin-Y stain for 15 seconds each. To wash away excess Eosin samples were placed in multiple changes of 95% EtOH (x2) and 100% EtOH (x3) for 1 minute each. Tissues were cleared in xylene, mounted in Cytoseal XYL, and left to dry overnight prior to imaging. Images were analyzed with NDP.view 2 software. The lesion and necrotic regions were outlined, and the areas were recorded. Areas were then averaged between sections of the same mouse and the

average lesion area per mouse was reported. Percent necrosis was then calculated by dividing the necrotic area by lesion area per mouse.

ORO staining and analysis.

Six sections spaced at 40 μm intervals were fixed (4% PFA, 10 min), washed, and dried with 60% isopropyl alcohol. Sections were stained with 0.3% ORO (20 min), rinsed with H_2O, counter-stained with Hematoxylin (1 min) and mounted in Gelvatol. Slides were imaged the same day or the following day. Images were analyzed with NDP.view 2 software. Regions of foam cells were measured for area and divided by the number of nuclei within that area. This was performed at 3-5 regions on all sections, averaged for each mouse and reported as average foam cell size/animal.

Sirius red staining and analysis.

Six sections spaced 40 μm intervals were fixed in 70% EtOH for 3 minutes, washed with diH_2O and stained in 0.1% Sirius red/Direct 80 saturated in an aqueous solution of picric acid for 1 hour. Tissues were then washed in two changes of 0.5% acetic acid for 5 minutes each, dehydrated in 100% EtOH for 30 seconds, and cleared with xylene for 2 minutes. Finally, slides were mounted with Cytoseal XYL and left to dry overnight prior to imaging. Images were analyzed with FIJI software. The percent collagen content was calculated by normalizing the collagen area to the lesion area and was reported per mouse. The plaque cap thickness was taken from 3-5 regions along each plaque and averaged per section. If no cap was present, then the thickness was recorded as 0.

Average cap thickness was then divided by the lesion area and was reported per mouse.

Imaging.

Lipid loaded C57BL/6 and εKO BMDM. Cells were imaged on an Olympus IX81-DSU spinning-disc confocal microscope at 60X oil with a Hamamatsu electron multiplying charge-coupled device camera, driven by MetaMorph software (Molecular Devices, Sunnyside, CA). Raw images were then processed using Imaris Software. Lipid loaded WT and mεKO BMDM. Cells were imaged on an Olympus BX51 microscope (Olympus, Tokyo, Japan) equipped with a QImaging Retiga 2000R digital camera (QImaging, Surrey, British Columbia, Canada) and CellSens software (Olympus Life Science, Waltham, MA). Images were collected with a 40X air objective. Raw images were processed using FIJI software. Aortic arches. Olympus SZ61 Dissecting Microscope equipped with an HD camera & monitor system from Excelis HDS was used to acquire images of aortic arches. Raw images were processed with FIJI software. Aortic roots. High-Speed, High-resolution Digital Slide Scanner. Hamamatsu NanoZoomer 2.0RS. Images were collected with a 40X air objective. Raw images were processed with NDP.view 2 or FIJI software.

Statistics.

Data are expressed as mean ± SEM of independent experiments or animals; *n* is noted in the figure legends. Comparison of means between groups was evaluated by one-way ANOVA, 2-tailed paired or unpaired students t-test, or Mann-Whitney U test. A p-value

less than 0.05 was considered statistically significant. All statistical analyses were performed using GraphPad Prism, SPSS, and R. Representative images were chosen based on those closest to the mean.

Study approval.

All animals received humane care in accordance with the NIH Guide for the Care and Use of Laboratory Animals. All procedures were approved by the Albany Medical Center Institutional Animal Care and Use Committee.

Data availability.

The public geneset data used to assess PRKCE read counts in early and advanced stages of atherosclerosis can be found on NCBI under GSE104140. Please see the Major Resources Table in the Supplemental Materials.

Results

Based on our work on PKCε in vesicular trafficking and phagocytosis (11), and the trafficking involved in the uptake of lipids and formation of foam cells, we hypothesized that MØ PKCε may be involved in the uptake of lipids. To test this, we incubated bone marrow-derived macrophages (BMDM) from wild type (C57BL/6) and PKCε knockout (εKO) mice with acetylated LDL (acLDL) and quantified the number and area of resulting lipid droplets. εKO BMDM contained significantly more,and larger lipid droplets (Figure 1A), implicating PKCε in lipid handling. Secondly, as atherosclerosis is a chronic inflammatory disease, we asked how PKCε expression affected inflammatory cytokine

release. We treated C57BL/6 and εKO BMDM with immune complexes to mimic the uptake of immune complexes present at high levels in humans with atherosclerosis (38, 39) and quantified release of TNFα and IL6, two cytokines linked to atherosclerosis. We found that secretion of TNFα , but not IL-6, was significantly higher in εKO cells (Figure 1B,C). This suggests that PKCε restricts TNFα, but not IL-6 release; differential secretion pathways for TNFα and IL6 have been reported, although the involvement of PKCε was not addressed (40). With εKO BMDM retaining more lipid and releasing more TNFα, it suggests PKCε limits foam cell formation and restricts the release of inflammatory cytokines, properties that would be protective, slowing the development of atherosclerosis.

To investigate the translational potential of our (mouse) results, we searched the literature for information on the expression of PKCε in human plaques. Unable to find data regarding the expression of PKCε *protein*, we assessed RNA sequencing data from endarterectomy specimens (GSE120521) for PRKCE. This NCBI geneset compared raw counts from early atheromas with diffuse intimal thickening with those from calcified or soft atheromas (late stage). Using R, raw counts of PRKCE per person were plotted and assessed for statistical differences. This data confirms that PKCε *is* expressed in human plaques and reveals that expression is decreased in more advanced lesions (Figure 2B; 41). While RNAseq of plaque tissue cannot identify the cell types with reduced PKCε, it suggests that PKCε may limit plaque progression and provides a rationale for examining how MØ PKCε affects atherosclerosis. Based on the human findings, we asked if hypercholesterolemia leads to decreased MØ PKCε. The recombinant adeno-associated viral vector serotype 8 – mouse proprotein convertase

subtilisin/kexin type 9 (AAV8-PCSK9) plus Western diet strategy (42) was used for inducing hypercholesterolemia (see Methods). After AAV8 injection, animals were maintained on the Western diet for 4 weeks; control animals received standard chow. Four days prior to harvesting, peritoneal macrophages (pMACs) were elicited by intraperitoneal (IP) thioglycolate injections. After harvesting, elicited pMACs RNA was prepared and PKCε expression was quantified by qPCR. This data revealed a significant decrease in PKCε in the lipid loaded pMACs compared to those from chow fed mice (Figure 2C). The lipid laden MØ having less PKCε parallels the human dataset (lower PKCε in advanced plaques), suggesting that plaque MØ have reduced PKCε expression in vivo.

LysMCre deletes PKCε from Macrophages. To study the effect of MØ PKCε on atherosclerosis, we crossed PKCε$^{fl/fl}$ mice (43) to LysMCre. LysMCre deletes flox'd genes in the myeloid lineage, primarily macrophages and neutrophils, with little to no effect on the lymphoid lineage (44). PKCε$^{fl/fl}$ females were paired with PKCε$^{fl/fl}$ LysMCre$^{+/-}$ males to produce PKCε$^{fl/fl}$ siblings that were LysMCre negative or hemizygous (Figure 3A).

To determine the efficiency of myeloid deletion, we compared PKCε protein expression across four mouse strains by western blot: C57BL/6 (parental, all cells positive), global PKCε knockout (εKO, all cells negative), PKCε$^{fl/fl}$ (designated WT, theoretically all cells positive), and PKCε$^{fl/fl}$ LysMCre$^{+/-}$ (designated mεKO: <u>m</u>yeloid selective PKC**<u>ε</u>** **<u>k</u>**nock**<u>o</u>**ut) (11). Brains and spleens were used as controls; brain because PKCε expression is highest in this tissue and spleens because the majority of cells are lymphoid so PKCε expression should not be affected by LysMCre. As

predicted, PKCε was expressed in brains and spleens of C57BL/6 mice but was undetectable in their εKO counterparts (Figure 3B). PKCε expression in WT and mεKO brains and spleens was not significantly different from C57BL/6 (Figure 3B) nor was mεKO expression significantly different from WT (i.e. PKCε$^{fl/fl}$). These results confirm the reported myeloid selectivity of LysMCre in the PKCε$^{fl/fl}$ background (Figure 3B).

The efficiency of PKCε deletion in MØ was determined by western blotting (Table 1). As predicted, BMDMs from mεKO mice had no detectable PKCε, similar to the εKO global knockouts (Figure 3C). PKCε expression in mεKO pMACs was reduced >85% compared to WT, a level not statistically different from mεKO BMDMs (Figure 3D). Thus, expression of PKCε in mεKO brains and spleens is similar to the parental C57BL/6 tissues. In contrast, PKCε in mεKO MØ is low/not expressed.

When genes are deleted, there may be compensation for the lost gene in the knockout animals. Thus, we compared the relative expression levels of PKCα, β, δ, η, ε, and ζ in BMDMs and found no significant differences between WT and mεKO except for in PKCε expression (Figure 4 A-F, Table 2). Thus, there is no obvious compensation for PKCε in mεKO animals.

Deletion of PKCε does not affect basal message levels of key atherosclerotic and inflammatory markers. qPCR was used to determine the effect of PKCε deletion on the expression of 25 genes implicated in atherosclerosis (45). There were no statistical differences in any of the markers tested (Supplementary Figure S1-4; Table 3,4). Flow cytometry confirmed no differences in the expression of scavenger receptors (SRA-1, CD206, CD36, and Dectin) or TLR 2,4 in either BMDM or pMACs; Lox-1 expression was below the levels of detection (Figure 5, Supplementary Figure S1, Table 5). Similarly, we

found no differences in FcγR and CD11b expression or that of MHCII and Ly6C, suggesting that PKCε deletion does not dramatically alter MØ polarization (Supplemental Figures S4D, S5). Thus, any plaque phenotype in mεKO animals is more likely due to signaling than intrinsic effects of differential receptor and inflammatory expression.

Lipid loaded MØs from mεKO mice retain more cholesterol. As MØ foam cells are a major feature of atheroscleroric lesions, and εKO BMDM retain more lipid than their C57BL/6 counterparts (Figure 1A), we asked if mεKO MØ had a lipid handling defect. WT and mεKO BMDMs were treated with or without human highly-oxidixed LDL (Hi-ox-LDL, 24 h). Lysates were then collected and quantified for the amount of retained total cholesterol (TC), free cholesterol (FC), and cholesterol esters (CE). The difference between TC and FC represents the amount of retained cholesterol esters (CE). mεKO BMDMs retain more TC and CE compared to WT (Figure 6A). These data parallel the results from εKO animals (Figure 1A). From these results we conclude that mεKO MØ retain more lipid; more foam cells may produce larger plaques.

Plaques from hypercholesterolemic mεKO mice are more advanced than WT. Knowing that MØ lacking PKCε retain more lipid (Figure 1,6A) and release more TNFα (Figure 1B), we hypothesized that loss of myeloid PKCε would exacerbate atherosclerosis *in vivo*. The AAV8-PCSK9 plus Western diet strategy (46) was used for inducing human-like hypercholesterolemia. All data was recorded by ear tag number such that the operator was blinded to genotype. Animals were injected with AAV8-PCKS9, started on the Western diet at 8 weeks old (T=0), and maintained on the diet for 16 weeks (T=16, Figure 6B). Weight was recorded at the start of the experiment and

prior to tissue harvesting. While weight increased with time, there were no significant genotype differences (Figure 6C). Likewise, plasma cholesterol (taken at weeks 2 and 16) increased with no genotype differences (Figure 6D); ≥500mg/dL of cholesterol was defined as hypercholesterolemic.

Plaque area was quantified in aortic arches and the aortic root. Aortic arches were stained with Oil red O (ORO) and lesion area normalized to arch area. Percent lesion coverage was significantly higher in mεKO aortic arches compared to WT, indicative of a higher plaque burden (Figure 7A,C). To test for inter-observer variability, two observers quantified a subset of the aortic arches; no significant variability was found (Figure 7B).

The aortic root lends itself to more detailed analyses. Sections were collected at the first sign of plaque near the aortic valve and sectioned such that each slide contained 3 x 10 μm sections at levels 250 μm apart (details in Methods). Six sections closest to the center of valves and 40 μm apart, were stained with Hematoxylin and Eosin (H&E). Consecutive slides were stained for ORO and picrosirius red.

H&E was used to determine lesion area and percent necrosis. Similar to the results from the descending aortas, we found that mεKO lesion area was significantly larger than WT. Secondly, we quantified regions of necrosis (H&E dull/devoid of nuclei) and found that mεKO plaques were significantly more necrotic (Figure 8A-C). Finally, we noted cholesterol clefts in mεKO plaques, indicating the inclusion of cholesterol crystals. While difficult to quantify, embedded cholesterol crystals are a hallmark of advanced plaques and few such inclusions were apparent in WT plaques (Figure 8A).

Consecutive sections were stained with ORO and picrosirius red to assess the amount and localization of lipid and collagen, respectively. ORO rich areas were quantified, normalized to the number of nuclei, and reported as average foam cell area/mouse (Figure 9). Consistent with results from in vitro lipid loading (Figure 1,6A), mεKO plaque foam cells have significantly more retained lipid, supporting the hypothesis that PKCε plays a role in lipid handling.

Aortic roots were stained with Picrosirius red to visualize collagen. The overall content was quantified and normalized to lesion area. Surprisingly, there was significantly *more* collagen in mεKO lesions compared to WT (Figure 10A,B). However, closer examination revealed that while the collagen overlayed the plaques in WT animals, much of it was submerged in mεKO samples. While mouse plaques do not tend to rupture, larger and more necrotic plaques are indicators of vulnerability in humans. However, rupture is less likely if the soft/necrotic core is protected by a thick fibrous cap. We found cap thickness to be significantly higher in WT; many mεKO plaques had regions with *no* cap indicating vulnerability (Figure 10A-C).

In summary, the overall composition of mεKO plaques (larger, more necrotic, engorged foam cells, embedded collagen overlayed with plaque, and significantly thinner caps) is consistent with human metrics of vulnerability. As the mεKO animals have PKCε deletion restricted to myeloid cells, we can conclude that loss of *myeloid* PKCε exacerbates the atherosclerotic program, identifying myeloid PKCε as a novel atheroprotective gene.

Discussion

PKCε has been shown to modulate diverse cellular processes including endothelial function, vascular smooth muscle cell migration, proliferation, and inflammation (23, 47, 48). Early work on PKCε in the immune system came from studies using the global PKCε knockout (εKO) mouse. εKO macrophages had blunted responses to LPS/IFNγ, including lower production of NO, TNFα, and IL-6. In infection studies, εKO mice succumbed to bacterial exposure while their wild type counterparts survived. This work uncovered a role for MØ PKCε in inflammation; failure to mount an effective inflammatory response to bacterial infection reduced survival (49).

PKCε has been shown to have context dependent effects depending on the cellular environment (50). Its role in atherosclerosis is unclear. On the one hand, MØ PKCε promotes inflammation and generates oxidative stress that leads to endothelial dysfunction and is pro-atherogenic (15, 22, 23, 26, 48). On the other hand, it has also been shown to have anti-atherogenic properties such as promoting smooth muscle cell (SMC) proliferation and migration for the development of a protective cap, influencing efficient lipid metabolism, and promoting cell survival by preventing apoptosis (16, 26, 47, 51-53). PKCε has been extensively studied in the context of ischemia-reperfusion, functioning in cardioprotection, and its role in atherosclerosis is implicated by its signaling in relevant cell types (21). This enzyme is an attractive target primarily because of its immunomodulatory function in disease and has been proposed as a therapeutic target in several diseases including cancer (down-regulation) and Alzheimer's disease (stimulation) (15, 8, 22, 23, 26, 32, 33, 47-49, 54, 55). These studies highlight the diverse role of PKCε in health and disease and that it may be

protective (cardioprotection) or destructive (tumor metastasis). Its expression at steady state may sustain homeostasis but its decrease or overexpression produces pathology.

Herein we sought to elucidate PKCε's isoform-specific function during atherogenesis, revealing regulatory mechanisms that may be exploited as potential therapeutic targets. Circulating IgG immune complexes are elevated in patients with atherosclerosis (38, 39, 56), and efficient IgG-mediated phagocytosis is PKCε dependent (11). Thus, we asked what effect immune complexes have on TNFα and IL-6 release. We discovered that TNFα, but not IL-6, release was substantially *higher* in εKO MØ, suggesting that PKCε *restricts* production of inflammatory mediators (Figure 1B,C). While initially surprising, this result could have been predicted based on the bioinformatics that revealed decreased PKCε expression in vulnerable plaques (Figure 2B) and our early work showing that TNFα message is elevated in vulnerable regions of human carotid plaques (57). Finally, we used MØ from global PKCε KO mice to ask if there was an obvious lipid handling defect. Upon acLDL feeding, we found that εKO BMDM retain more lipid. This was confirmed and extended by treating WT and mεKO BMDMs with (human) Hi-ox-LDL (Figure 1A,6A). Finally, we interrogated an RNAseq human database of early and advanced plaques and found that PKCε is significantly reduced in advanced plaques (Figure 2B). Extending this to mice, we found that MØ from hypercholesterolemic mice have significantly lower PKCε expression than their chow fed counterparts (Figure 2C). Taken together, these data provide in vivo and in vitro evidence, from both mice and humans, that PKCε is decreased, and TNFα is increased, in vulnerable human plaques and hypoercholesterolemic mice. With murine MØ lacking PKCε releasing more TNFα and retaining more lipids suggests the

expression of PKCε in MØ may slow atherosclerosis progression. This provides the rationale for asking how MØ PKCε expression impacts atherosclerosis in vivo.

As atherosclerosis is a lipid-driven chronic inflammatory disease in which MØ are major players, MØ PKCε could promote and/or restrict plaque development. Using the global PKCε knockout mice for these studies presented two major roadblocks, both practical and experimental. Practically, the global knockouts were significantly smaller, less hearty, and were not produced in Mendelian proportions. Animals had to be bred as heterozygotes due to the uterine infections in female mice, pointing to systemic defect effects (49). Experimentally, our focus is on the role of *MØ PKCε* on atherosclerosis. A global knockout has PKCε deleted from all cells, including those that contribute to atherosclerosis (eg, endothelium, smooth muscle cells). Thus, any resulting phenotype could not be conclusively linked to myeloid cells. To circumvent these roadblocks, we produced the mεKO mouse.

mεKO mice are indistinguishable from their WT counterparts. Breeding male LysMCre hemizygotes to LysMCre negative females produced litters of 7-13 animals that were approximately 50% LysMCre$^{+/-}$ making it relatively easy to generate sufficient numbers of each genotype for the atherosclerosis cohorts (Figure 3A). To confirm the selectivity of the LysMCre on myeloid deletion, we produced a small colony of animals on the Zs green reporter background. Anaysis of blood and spleen by flow cytometry confirmed that neutrophils and monocytes (blood), but not B and T cells (spleen), were Zs Green positive. By Western blotting, the relative expression of PKCε in the brain and spleen of mεKO mice was indistinguishable from parental C57BL/6 mice or the Cre negative PKCε$^{fl/fl}$ (“WT”), confirming that neither the floxed gene alone nor LysMCre

expression altered basal PKCε expression in these tissues (Figure 3B). Notably, the absence of PKCε signal in tissues from the global εKO validated the specificity of the PKCε antibody. PKCε protein expression in BMDMs and elicited pMACs were significantly decreased in mεKO suggesting selective and effective deletion of PKCε in MØ. As expected, there was no difference between the level of relative PKCε protein expression between BMDMs and pMACs (Figure 3C,D). Even though there is significantly less PKCε expression in mεKO pMACs compared to WT, a light band is consistently detected. We hypothesize this is due to pMACs having a mixed population of cells; this signal may be from peritoneal B-1A cells that express high levels of PKCε (ImmGen Probe Set 10447294).

The homology of the PKC catalytic domains suggests that there could be compensation for the loss of PKCε by upregulation of another isoform. That does not seem to be the case as there are no differences in the expression of other PKC isoforms in meKO MØ (Figure 4). Additionally, the unique substrate specificity of PKCε (14, 42, 49, 58) would make functional compensation difficult. Given the lack of compensation for PKCε loss, we hypothesize that it is PKCε *signaling* that limits atherosclerosis in WT animals.

PKCε knockout MØ retain more cholesterol and have more lipid droplets (Figure 1A). These are global knockouts so it is possible that the phenotype is a function of the overall loss of PKCε. Indeed, the global knockout animals are more fragile and have reproductive and immunological deficits (49). However, the phenotype was recapitulated in MØ from mεKO mice that retain significantly more cholesterol than their WT counterparts (Figure 6A). Thus, we conclude that the elevated lipid levels in εKO MØ

are related to the loss of PKCε. How PKCε regulates lipid uptake and/or efflux is currently an open question.

To test the hypothesis that myeloid PKCε plays a role in atherosclerosis, we exploited the AAV8-PCSK9 plus Western diet strategy that enabled us to produce sustained hypercholesterolemia in our animals without crossing to the ApoE or LDLR background (42). Doing so combats the confounding effects of these traditional murine atherosclerotic models (44, 46, 59). Also, these studies were done with males because atherosclerosis disproportionately affects males vs pre-menopausal women (60). As 8-24 weeks in mice correspond to ~15-25 years in humans (61), and mice undergo changes similar to menopause at 9-12 months (62), female mice are still cycling at 8-24 weeks. It should be noted that males and females were included in the first cohort, however, the females did not remain hypercholesterolemic and did not produce plaques. Additionally, the response of female mice to AAV8-PCSK9 strategy is lower than males; therefore, the virus will be titrated to ensure long-term hypercholesterolemia before determining the effect of sex on plaque progression in mεKO mice (63).

Human vulnerable plaques present with thin fibrous caps, regions of necrosis, and lipid inclusions. These are the same metrics we used to phenotype the murine aortic root plaques. mεKO plaques were larger, more necrotic, and surprisingly contained more collagen than WT (Figure 8-10). In humans, superficial collagen protects the necrotic core and stabilizes the plaque. Conversely, collagen buried beneath a layer of foam cells exposes the foam cells to the vessel lumen, thereby increasing the likelihood of plaque rupture (64). Cap thickness is a critical indicator of stability in humans (65); mεKO plaques had buried collagen with overlaying foam cells

and significantly thinner caps. In some cases, the vulnerable shoulder regions had no overlying collagen (Figure 10). An additional indicator of plaque vulnerability is the inclusion of cholesterol crystals (63); cholesterol clefts, the skeleton of cholesterol crystals, were evident in H&E stained mεKO plaques, but not WT, animals (Figure 8A). In summary, despite the fact that murine plaques don't rupture, these features in humans (especially the thin/no cap overlaying a necrotic plaque) would be an indicator of future rupture. By these criteria, we conclude that PKCε expression in MØ produces smaller, more stable plaques, identifying it as a novel atheroprotective gene. Finally, our model has translational potential in that PKCε expression is lower in advanced human plaques and MØ from hypercholesterolemic mice (41); Figure 2B,C).

The dramatic differences between mεKO and WT plaques suggest that MØ PKCε occupies a critical node in the atherosclerosis signaling network. How it acts to restrict TNFα release, limit intracellular cholesterol, reduce the formation of necrotic cores, and support maintenance of a collagen cap are open questions. One conundrum may provide some insight; during IgG-mediated phagocytosis, PKCε mediates the delivery of Golgi-derived vesicles to the forming phagosome (11). Those vesicles carry TNFα and are not delivered in εKO MØ (11). How then, does *loss* of PKCε lead to *more* TNFα secretion? The answer may lie in vesicular trafficking, where there is a sorting of cargo for secretion. Murray and Stow showed this elegantly using cytokines and identifying SNAREs and Rabs that regulate differential secretion of TNFα, IL6, and IL10 (40). We have shown PKCε mediates focal exocytosis during IgG-mediated phagocytosis (11). In PKCε KO cells, this pathway could be blocked, shunting TNFα to constitutive pathways, resulting in more TNFα release and a more inflammatory plaque

environment. Thus, PKCε may dampen the inflammatory response which would slow plaque progression. This hypothesis is supported by the RNAseq data (Figure 2B) showing reduced PKCε in soft/late plaques and increased TNFα in vulnerable regions of human plaques (57).

Finally, we can draw on the cancer literature to provide clues as to how MØ PKCε might reduce apoptosis to limit necrosis. PKCε is overexpressed in many cancers. Overexpression increases tumor cell migration and reduces apoptosis (32-37). In atherosclerosis, PKCε could facilitate monocyte migration into fatty streaks, allowing for more removal and efflux of intimal lipid. If expression of PKCε in MØ is anti-apoptotic, we would expect less necrosis in WT plaques (Figure 8A,C). On the other hand, as necrosis results when efferocytosis is compromised, PKCε could facilitate efferocytosis. The effect of PKCε on efferocytosis remains to be determined.

Finally, it should be noted that a missing piece to the "PKCε in atherosclerosis puzzle" is its role in resolution. Resolution of inflammation is an active process mediated by pro-resolving lipid mediators. A model for studying the inflammation → resolution axis in vivo has been published (20) and will be used to identify where PKCε acts during resolving inflammation. In summary, this work uncovered a new player in atherogenesis. Understanding *how* MØ PKCε slows plaque progression is our ongoing challenge.

Supplemental Material

Figure S1-S5

Major Resources Table

Acknowledgments

The authors thank Dr. Gabrielle Fredman for her expertise in atherosclerosis and constructive feedback on experimental design and Dr. Younghwa Goo for help with cholesterol assays. The authors would also like to thank Genome Editing and Animal Models Core at the University of Wisconsin (Madison) Biotechnology Center for supplying the PKCε$^{fl/fl}$ sperm, Taconic Biosciences (Rensselaer, NY) for producing PKCε$^{fl/fl}$ mice, Cheryl Zjad for doing the initial animal husbandry and aiding in the development of the PKCε$^{fl/fl}$ LysMCre murine line, Rosemary Prestipino for assisting in the creation of the graphical abstract, Albany Medical College's Bioinformatic Core for producing graphs from RNA sequencing data, and BioRender for aiding in diagram development. ATW backcrossed the PKCε$^{fl/fl}$ mice to generate the congenic strain for Jackson Labs (B6(Cg)-*Prkce*$^{tm1.1Akv}$/LennMmjax stock# 69556), maintained the LysM Cre PKCε$^{fl/fl}$ colony, designed and conducted experiments, analyzed the data, and wrote the manuscript. MMS processed and analyzed the aortic arch tissue and ran qPCR. RHB processed MØ and ran qPCR. AED ran and analyzed experiments using the global (εKO) knockout MØ. RBR managed and analyzed NCBI's geneset GSE104140. MRL coordinated the research, provided the funding, ran and analyzed flow cytometry, and wrote the manuscript.

Sources of Funding

This work was supported by R03 AI144841, Johnathan Vasiliou Foundation, and Albany Medical College Bridge Funds.

Disclosures

None.

REFERENCES

1. What is Cardiovascular Disease. https://www.heart.org/en/health-topics/consumer-healthcare/what-is-cardiovascular-disease.
2. Di Cesare M, Perel P, Taylor S, Kabudula C, Bixby H, Gaziano TA, et al. The Heart of the World. *Glob Heart.* 2024;19(1):11.
3. Heart Disease Facts. https://www.cdc.gov/heart-disease/data-research/facts-stats/index.html.
4. Liu Y, Yuan J, Tan T, Jia W, Lugea A, Mareninova O, et al. Genetic inhibition of protein kinase Cε attenuates necrosis in experimental pancreatitis. *Am J Physiol Gastrointest Liver Physiol.* 2014;307(5):G550-63.
5. Tabas I, García-Cardeña G, and Owens GK. Recent insights into the cellular biology of atherosclerosis. *J Cell Biol.* 2015;209(1):13-22.
6. Hafiane A. Vulnerable Plaque, Characteristics, Detection, and Potential Therapies. *J Cardiovasc Dev Dis.* 2019;6(3).
7. Bobryshev YV, Ivanova EA, Chistiakov DA, Nikiforov NG, and Orekhov AN. Macrophages and Their Role in Atherosclerosis: Pathophysiology and Transcriptome Analysis. *Biomed Res Int.* 2016;2016:9582430.
8. Petersen C, Peçanha PB, Venneri L, Pasanisi E, Pratali L, and Picano E. The impact of carotid plaque presence and morphology on mortality outcome in cardiological patients. *Cardiovasc Ultrasound.* 2006;4:16.
9. Kasikara C, Doran AC, Cai B, and Tabas I. The role of non-resolving inflammation in atherosclerosis. *J Clin Invest.* 2018;128(7):2713-23.

10. Moore KJ, and Tabas I. Macrophages in the pathogenesis of atherosclerosis. *Cell.* 2011;145(3):341-55.

11. D'Amico AE, Wong AC, Zajd CM, Zhang X, Murali A, Trebak M, et al. PKC-ε regulates vesicle delivery and focal exocytosis for efficient IgG-mediated phagocytosis. *J Cell Sci.* 2021;134(21):jcs258886.

12. Hanes CM, D'Amico AE, Ueyama T, Wong AC, Zhang X, Hynes WF, et al. Golgi-Associated Protein Kinase C-ε Is Delivered to Phagocytic Cups: Role of Phosphatidylinositol 4-Phosphate. *J Immunol.* 2017;199(1):271-7.

13. Larsen EC, Ueyama T, Brannock PM, Shirai Y, Saito N, Larsson C, et al. A role for PKC-epsilon in Fc gammaR-mediated phagocytosis by RAW 264.7 cells. *J Cell Biol.* 2002;159(6):939-44.

14. Wood TR, Chow RY, Hanes CM, Zhang X, Kashiwagi K, Shirai Y, et al. PKC-ε pseudosubstrate and catalytic activity are necessary for membrane delivery during IgG-mediated phagocytosis. *J Leukoc Biol.* 2013;94(1):109-22.

15. Poolman TM, Quinn PA, and Ng L. Protein Kinase C Epsilon Contributes to NADPH Oxidase Activation in a Pre-Eclampsia Lymphoblast Cell Model. *Diseases.* 2013;1(1):1-17.

16. Reyland ME. Protein kinase C isoforms: Multi-functional regulators of cell life and death. *Front Biosci (Landmark Ed).* 2009;14(6):2386-99.

17. Larsen EC, DiGennaro JA, Saito N, Mehta S, Loegering DJ, Mazurkiewicz JE, et al. Differential requirement for classic and novel PKC isoforms in respiratory burst and phagocytosis in RAW 264.7 cells. *J Immunol.* 2000;165(5):2809-17.

18. Crane MJ, Daley JM, van Houtte O, Brancato SK, Henry WL, Jr., and Albina JE. The monocyte to macrophage transition in the murine sterile wound. *PLoS One.* 2014;9(1):e86660.

19. Tabas I. Macrophage apoptosis in atherosclerosis: consequences on plaque progression and the role of endoplasmic reticulum stress. *Antioxid Redox Signal.* 2009;11(9):2333-9.

20. Fredman G, Li Y, Dalli J, Chiang N, and Serhan CN. Self-limited versus delayed resolution of acute inflammation: temporal regulation of pro-resolving mediators and microRNA. *Sci Rep.* 2012;2:639.

21. Chen L, Shi D, and Guo M. The roles of PKC-d and PKC-e in myocardial ischemia/reperfusion injury. *Pharmacol Res.* 2021;170:105716.

22. Zuniga MC, Raghuraman G, Hitchner E, Weyand C, Robinson W, and Zhou W. PKC-epsilon and TLR4 synergistically regulate resistin-mediated inflammation in human macrophages. *Atherosclerosis.* 2017;259:51-9.

23. Inagaki K, Churchill E, and Mochly-Rosen D. Epsilon protein kinase C as a potential therapeutic target for the ischemic heart. *Cardiovasc Res.* 2006;70(2):222-30.

24. Palaniyandi SS, Sun L, Ferreira JC, and Mochly-Rosen D. Protein kinase C in heart failure: a therapeutic target? *Cardiovasc Res.* 2009;82(2):229-39.

25. Saurin AT, Pennington DJ, Raat NJH, Latchman DS, Owen MJ, and Marber MS. Targeted disruption of the protein kinase C epsilon gene abolishes the infarct size reduction that follows ischaemic preconditioning of isolated buffer-perfused mouse hearts. *Cardiovasc Res.* 2002;55(3):672-80.

26. Lien CF, Chen SJ, Tsai MC, and Lin CS. Potential Role of Protein Kinase C in the Pathophysiology of Diabetes-Associated Atherosclerosis. *Front Pharmacol.* 2021;12:716332.

27. Mehta KD, Radominska-Pandya A, Kapoor GS, Dave B, and Atkins BA. Critical role of diacylglycerol- and phospholipid-regulated protein kinase C epsilon in induction of low-density lipoprotein receptor transcription in response to depletion of cholesterol. *Mol Cell Biol.* 2002;22(11):3783-93.

28. Waza AA, Andrabi K, and Hussain MU. Protein kinase C (PKC) mediated interaction between conexin43 (Cx43) and K(+)(ATP) channel subunit (Kir6.1) in cardiomyocyte mitochondria: Implications in cytoprotection against hypoxia induced cell apoptosis. *Cell Signal.* 2014;26(9):1909-17.

29. Singh RK, Haka AS, Asmal A, Barbosa-Lorenzi VC, Grosheva I, Chin HF, et al. TLR4 (Toll-Like Receptor 4)-Dependent Signaling Drives Extracellular Catabolism of LDL (Low-Density Lipoprotein) Aggregates. *Arterioscler Thromb Vasc Biol.* 2020;40(1):86-102.

30. Faisal A, Saurin A, Gregory B, Foxwell B, and Parker PJ. The scaffold MyD88 acts to couple protein kinase Cepsilon to Toll-like receptors. *J Biol Chem.* 2008;283(27):18591-600.

31. Ross AM, Gibbons RJ, Stone GW, Kloner RA, and Alexander RW. A randomized, double-blinded, placebo-controlled multicenter trial of adenosine as an adjunct to reperfusion in the treatment of acute myocardial infarction (AMISTAD-II). *J Am Coll Cardiol.* 2005;45(11):1775-80.

32. Gorin MA, and Pan Q. Protein kinase C epsilon: an oncogene and emerging tumor biomarker. *Mol Cancer.* 2009;8:9.

33. He S, Li Q, Huang Q, and Cheng J. Targeting Protein Kinase C for Cancer Therapy. *Cancers (Basel).* 2022;14(5):1104.

34. Casado-Medrano V, Baker M, J., Cooke M, and Kazanietz MG. Mechanisms of protein kinase C epsilon down-regulation by transforming growth factor-beta in lung cancer cells. *bioR$_x$iv.* 2020:2.

35. Nicholson R, Menezes AC, Azevedo A, Leckenby A, Davies S, Seedhouse C, et al. Protein kinase C epsilon overexpression is associated with poor patient outcomes in AML and promotes Daunorubicin resistance through p-glycoprotein-mediated drug efflux. *Front Oncol.* 2022;12:840046.

36. Sivaprasad U, Shankar E, and Basu A. Downregulation of Bid is associated with PKCepsilon-mediated TRAIL resistance. *Cell Death Differ.* 2007;14(4):851-60.

37. Huang B, Cao K, Li X, Guo S, Mao X, Wang Z, et al. The expression and role of protein kinase C (PKC) epsilon in clear cell renal cell carcinoma. *J Exp Clin Cancer Res.* 2011;30(1):88.

38. Sobenin IA, Salonen JT, Zhelankin AV, Melnichenko AA, Kaikkonen J, Bobryshev YV, et al. Low density lipoprotein-containing circulating immune complexes: role in atherosclerosis and diagnostic value. *Biomed Res Int.* 2014;2014:205697.

39. Wolf D, and Ley K. Immunity and Inflammation in Atherosclerosis. *Circ Res.* 2019;124(2):315-27.

40. Murray RZ, and Stow JL. Cytokine Secretion in Macrophages: SNAREs, Rabs, and Membrane Trafficking. *Front Immunol.* 2014;5:538.

41. Transcriptome sequencing of human fibroatheromas identifies genetic signature of plaque formation and suggests roles of TREM1 and PIK3CG in atherosclerosis. https://www.ncbi.nlm.nih.gov/geo/query/acc.cgi?acc=GSE104140.

42. Keeter WC, Carter NM, Nadler JL, and Galkina EV. The AAV-PCSK9 murine model of atherosclerosis and metabolic dysfunction. *Eur Heart J Open.* 2022;2(3):oeac028.

43. Hafeez BB, Zhong W, Weichert J, Dreckschmidt NE, Jamal MS, and Verma AK. Genetic ablation of PKC epsilon inhibits prostate cancer development and metastasis in transgenic mouse model of prostate adenocarcinoma. *Cancer Res.* 2011;71(6):2318-27.

44. Abram CL, Roberge GL, Hu Y, and Lowell CA. Comparative analysis of the efficiency and specificity of myeloid-Cre deleting strains using ROSA-EYFP reporter mice. *J Immunol Methods.* 2014;408:89-100.

45. Stöger JL, Gijbels MJ, van der Velden S, Manca M, van der Loos CM, Biessen EA, et al. Distribution of macrophage polarization markers in human atherosclerosis. *Atherosclerosis.* 2012;225(2):461-8.

46. Xu M, Wu X, Liu Z, Ding Y, Kong W, Little PJ, et al. A novel mouse model of diabetes, atherosclerosis and fatty liver disease using an AAV8-PCSK9-D377Y injection and dietary manipulation in db/db mice. *Biochem Biophys Res Commun.* 2022;622:163-9.

47. Ringvold HC, and Khalil RA. Protein Kinase C as Regulator of Vascular Smooth Muscle Function and Potential Target in Vascular Disorders. *Adv Pharmacol.* 2017;78:203-301.

48. Capuani B, Pacifici F, Pastore D, Palmirotta R, Donadel G, Arriga R, et al. The role of epsilon PKC in acute and chronic diseases: Possible pharmacological implications of its modulators. *Pharmacol Res.* 2016;111:659-67.

49. Castrillo A, Pennington DJ, Otto F, Parker PJ, Owen MJ, and Boscá L. Protein kinase Cepsilon is required for macrophage activation and defense against bacterial infection. *J Exp Med.* 2001;194(9):1231-42.

50. Jain K, and Basu A. The Multifunctional Protein Kinase C-ε in Cancer Development and Progression. *Cancers (Basel).* 2014;6(2):860-78.

51. Singh RM, Cummings E, Pantos C, and Singh J. Protein kinase C and cardiac dysfunction: a review. *Heart Fail Rev.* 2017;22(6):843-59.

52. Miao LN, Pan D, Shi J, Du JP, Chen PF, Gao J, et al. Role and Mechanism of PKC-δ for Cardiovascular Disease: Current Status and Perspective. *Front Cardiovasc Med.* 2022;9:816369.

53. Ding L, Wang H, Lang W, and Xiao L. Protein kinase C-epsilon promotes survival of lung cancer cells by suppressing apoptosis through dysregulation of the mitochondrial caspase pathway. *J Biol Chem.* 2002;277(38):35305-13.

54. Pan Q, Bao LW, Kleer CG, Sabel MS, Griffith KA, Teknos TN, et al. Protein kinase C epsilon is a predictive biomarker of aggressive breast cancer and a validated target for RNA interference anticancer therapy. *Cancer Res.* 2005;65(18):8366-71.

55. Sen A, Nelson TJ, Alkon DL, and Hongpaisan J. Loss in PKC Epsilon Causes Downregulation of MnSOD and BDNF Expression in Neurons of Alzheimer's Disease Hippocampus. *J Alzheimers Dis.* 2018;63(3):1173-89.

56. Lopes-Virella MF, Binzafar N, Rackley S, Takei A, La Via M, and Virella G. The uptake of LDL-IC by human macrophages: predominant involvement of the Fc gamma RI receptor. *Atherosclerosis.* 1997;135(2):161-70.

57. Lennartz MR, Aggarwal A, Michaud TM, Feustel PJ, Jones DM, Brosnan MJ, et al. Ligation of macrophage Fcγ receptors recapitulates the gene expression pattern of vulnerable human carotid plaques. *PLoS One.* 2011;6(7):e21803.

58. Schaap D, Parker PJ, Bristol A, Kriz R, and Knopf J. Unique substrate specificity and regulatory properties of PKC-epsilon: a rationale for diversity. *FEBS Lett.* 1989;243(2):351-7.

59. Oppi S, Lüscher TF, and Stein S. Mouse Models for Atherosclerosis Research-Which Is My Line? *Front Cardiovasc Med.* 2019;6:46.

60. Poznyak AV, Sukhorukov VN, Guo S, Postnov AY, and Orekhov AN. Sex Differences Define the Vulnerability to Atherosclerosis. *Clin Med Insights Cardiol.* 2023;17:11795468231189044.

61. Wang S, Lai X, Deng Y, and Song Y. Correlation between mouse age and human age in anti-tumor research: Significance and method establishment. *Life Sci.* 2020;242:117242.

62. Diaz Brinton R. Minireview: translational animal models of human menopause: challenges and emerging opportunities. *Endocrinology.* 2012;153(8):3571-8.

63. Shi X, Cai H, Wang F, Liu R, Xu X, Li M, et al. Cholesterol Crystals are Associated with Carotid Plaque Vulnerability: An Optical Coherence Tomography Study. *J Stroke Cerebrovasc Dis.* 2020;29(2):104579.

64. Libby P. Inflammation in atherosclerosis. *Nature.* 2002;420(6917):868-74.

65. Maiolino G, Rossitto G, Caielli P, Bisogni V, Rossi GP, and Calò LA. The role of oxidized low-density lipoproteins in atherosclerosis: the myths and the facts. *Mediators Inflamm.* 2013;2013:714653.

66. Vozenilek AE, Blackburn CMR, Schilke RM, Chandran S, Castore R, Klein RL, et al. AAV8-mediated overexpression of mPCSK9 in liver differs between male and female mice. *Atherosclerosis.* 2018;278:66-72.

67. Harmon EY, Fronhofer V, 3rd, Keller RS, Feustel PJ, Zhu X, Xu H, et al. Anti-inflammatory immune skewing is atheroprotective: Apoe−/−FcγRIIb−/− mice develop fibrous carotid plaques. *J Am Heart Assoc.* 2014;3(6):e001232.

Highlights:

- A novel murine model in which PKCε is floxed (PKCε$^{fl/fl}$) on both alleles haas been generated, backcrossed, and deposited into Jackson Laboratories.
- PKCε$^{fl/fl}$ mice have been crossed with those on the LysM Cre background thereby deleting PKCε from myeloid cells (mεKO).
- Deletion of PKCε has no basal affects on other PKC isoforms, lipid handling markers, or inflammatory markers.
- Upon stimulation with lopid loading in vitro or hypercholesterolemia in vivo, mεKO BMDMs retain more cholesterol and mεKO mice develop a more vulnerable plaque phenotype (i.e. larger lesions, more necrosis, thimmer plaque caps).
- These findings provide a rationale for the need to identify mediators in the PKCε signaling pathway responsible for protection against vulnerable plaques in atherosclerosis; potentially aiding in the development of preventative and therapeutic treatments.

Table 1. Western blot Antibodies and Dilution Factor

Antibody	Type	Vendor and Catalog Number	Dilution Factor
PKC-epsilon	Rabbit pAb	Millipore-Sigma #06-991	1:500
GAPDH	Rabbit mAb	Cell Signaling #2118	1:1,000
Secondary	Goat anti-rabbit HRP (highly cross-adsorbed)	ThermoFisher Scientific #A16110	1:10,000

Primary and secondary antibodies used for Western blotting. Western blots for PKCε and GAPDH in BMDMs. n=3-6. No substantive differences between C57BL/6 and WT (PKCε$^{fl/fl}$), or in mεKO brains and spleens. Substantive deletion in εKO in all samples, however mεKO was only substantively deleted within BMDMs and pMACs. Figure 4. ANOVAs or unpaired T-tests were run, mean and SEM is plotted, *$p<0.05$. Antibodies are listed with their antibody type, catalog number, and dilution factor.

Table 2. RT-qPCR Primer and Sequences and p-values for PKC Isoforms

Name	Sequence	BMDM p-value
β-actin	TCGCCTGAGGCTCTTTTCC AGTTTCATGGATGCCACAGGAT	-
PKCε	GGGGTGTCATAGGAAAACAGG GACGCTGAACCGTTGGGAG	0.01
PKCη	TCCGGCACGATGAAGTTCAAT TACGCTCACCGTCAGGTAGG	0.90
PKCδ	ACATTCTGCGGCACTCCTGACT CCGATGAGCATTTCGTACAGGAG	0.93
PKCα	ACAACCTGGACAGAGTGAAACTC CTTGATGGCGTACAGTTCCTCC	0.54
PKCβ	CCAAGATGACGATGTGGAGTGC CTCCATCACAAAGTACAGGCGG	0.70
PKCζ	GGCAGAGAAAACTTCCAGAGGAG ATGTGTCCGTCGGCATCAAGGA	0.81

Deletion of PKCε Does Not Result in Apparent Compensation. qPCR for PKCε, PKCη, PKCδ, PKCα, PKCβ, and PKCζ in BMDMs. n=5-8. No substantive differences between genotypes besides within PKCε. Figure 4. Unpaired T-test were run, mean and SEM is plotted, *p<0.05. Primers are listed with their corresponding sequence and resulting p-value.

Table 3. RT-qPCR Primer Sequences and p-vales for Lipid Handling Markers

Name	Sequence Forward/Reverse	BMDM p-value	pMAC p-value
β-actin	TCGCCTGAGGCTCTTTTCC AGTTTCATGGATGCCACAGGAT	-	-
CD36	GCCTCCTTTCCACCTTTTGTT CGTAGATAGACCTGCAAATGTCAGA	0.95	0.35
Lox-1	GGTTCCCTGCTGCTATGACTCT GGCGTAATTGTGTCCACTGTACA	0.13	0.51
SRA-I	CAGACTGAAGGACTGGGAACACT GGAGGCCCTTGAATGAAGGT	0.82	0.60
CD206	GGATGTTGATGGCTACTGGAGAA GGGATTTCGTCTGATTTTTTGC	0.40	0.63
LDLR	CCAGACCCAGAGCCATCGTA CGGGTGTTCCCCAATCTGT	0.95	>0.99
VLDLR	CATCCTTCCTCTCTTGCTCTTAGTG GCCAATTCCTCCACATCAAGTAG	0.89	0.17
TLR2	CCCATTGAGAGGAAAGCCATT CTCCAGGTAGGTCTTGGTGTTCA	0.12	0.40
TLR4	CTTTATTCAGAGCCGTTGGTGTATC CCAGAGCGGCTGCTCAGA	0.82	0.42
Dectin-1	ACAATGCTGGCAACTGGGCTCT AGAGCCATGGTACCTCAGTCTG	0.87	0.39
ABCA1	GGGTGGTGTTCTTCCTCATTACTG TTTACAGGTCTGGGCCTGATG	0.69	0.65
ABCG1	GACACCGATGTGAACCCGTTTC GCATGATGCTGAGGAAGGTCCT	0.28	0.92

Deletion of PKCε Does Not Affect Basal Message of Key Lipid Uptake and Efflux Transporters. qPCR for CD36, Lox-1, SRA-I, CD206, LDLR, VLDLR, TLR2, TLR4, Dectin-1, ABCA1, ABCG1 in both BMDMs and elicited pMACs. n=3-7. No substantive differences between genotypes. Figure 5, Supplemental Figure 1. Unpaired T-test were run, mean and SEM is plotted, *p<0.05. Primers are listed with their corresponding sequence and resulting p-value.

Table 4. RT-qPCR Primer Sequences and p-values for Inflammatory markers

Name	Sequence	BMDM p-value	pMAC p-value
β-actin	TCGCCTGAGGCTCTTTTCC AGTTTCATGGATGCCACAGGAT	-	-
iNOS	TGGAGCGAGTTGTGGATTGTC CCAGTAGCTGCCGCTCTCAT	0.40	0.7
TNF-α	CATCTTCTCAAAATTCGAGTGACAA TGGGAGTAGACAAGGTACAACCC	0.66	0.40
IL-12 p40	CATCAGGGACATCATCAAACCA TGACCTCCACCTGTGAGTTCTTC	0.54	0.24
IFN-γ	GGATGCATTCATGAGTATTGC CCTTTTCCGCTTCCTGAGG	0.31	0.40
CD86	TGTTCTGGAAACGGAGTCAATG GGAGATGGAAACTCTTGAGTGAAATT	0.92	0.44
IL-6	GCCAGAGTCCTTCAGAGAG GGTCCTTAGCCACTCCTTC	0.69	>0.99
IL-17A	GGACTCTCCACCGCAATGAA GCACTGAGCTTCCCAGATCAC	0.42	0.49
COX-2	TCATTCACCAGACAGATTGCTGG TCCAAGCTCTACCATGGTCTCC	0.59	0.27
IL-1β	AGATGAACAACAAAAAAGCC TCTATCTTGTTGAAGACAAACC	0.36	0.63
Arg-I	GTCTGGCAGTTGGAAGCATCA TGTGAGCATCCACCCAAATG	0.35	0.40
TGFβ-1	TGAACCAAGGAGACGGAATACA GGAGTTTGTTATCTTTGCTGTCACAA	0.82	0.60
IL-10	GATTTTAATAAGCTCCAAGACCAAGGT TTCTATGCAGTTGATGAAGATGTCAA	0.93	0.44
MHCII	TCTGTCCTGGTGGCTCTG TGGACGCATCAGCAAGGG	0.73	0.40

Deletion of PKCε Does Not Affect Basal Message of Key Inflammatory Markers. qPCR for iNOS, TNF-α, IL-12 p40, IFN-γ, CD86, IL-6, IL-17A, COX-2, IL-1β, Dectin-1, Arg-I, TGFβ-1, IL-10, and MHC-II in both BMDMs and elicited pMACs. n=3-6. No substantive differences between genotypes. Supplemental Figure 1. Unpaired T-test were run. Mean and SEM is plotted, *p<0.05. Primers are listed with their corresponding sequence and resulting p-value.

Table 5. Flow Antibodies and Dilution Factor

Antibody	Fluorochrome	Vendor and Catalog Number	Clone	Ab Dilution (μl/5x10^5 C*)
CD11b	SBV515	Bio-Rad #MCA711SBV515	5C6	2
CD16.2	Biotin	BioLegend #149512	9.00E+09	2
CD16/32	BV421	BD Biosciences #562896	2.4g2	1
CD204/SRA-1	APC	BioLegend #102610	HM36	2.5
CD206/SRE-3	Biotin	LifeTech #MA5-16869	MR5D3	2
CD36/SRB-2	A700	Bio-Rad #MCA2748A700	MF3	2.5
CD64	A647	R & D Systems #FAB20741R	290322	1
Dectin-1/SRE-2	PE	Bio-Rad #MCA2289PE	2A11	2.5
Lox-1/SRE-1	Alexa 405	R & D Systems #FAB1564V	21402	2.5
Ly6C	SBV515	Bio-Rad #MCA2389SBV515	ER-MP20	2
MHCII	SB780	LifeTech #78-5321-82	M5/114.15.2	0.05
Streptavidin	SBV790	Bio-Rad #STAR210SBV790	Ø	1
TLR2	PE	LifeTech #12-9021-80	6C2	0.05
TLR4	PE-Cy7	BioLegend #145407	SA15-21	1

Deletion of PKCε Does Not Affect the Surface Expression of Key Lipid and Inflammatory Receptors. Flow of BMDMs for common dysregulated receptors in atherosclerosis. n=2-5. No substantive differences between genotypes. Figure 5, Supplemental Figure 2. Antibodies are listed with their catalog and clone ID's along with their corresponding dilution factor.

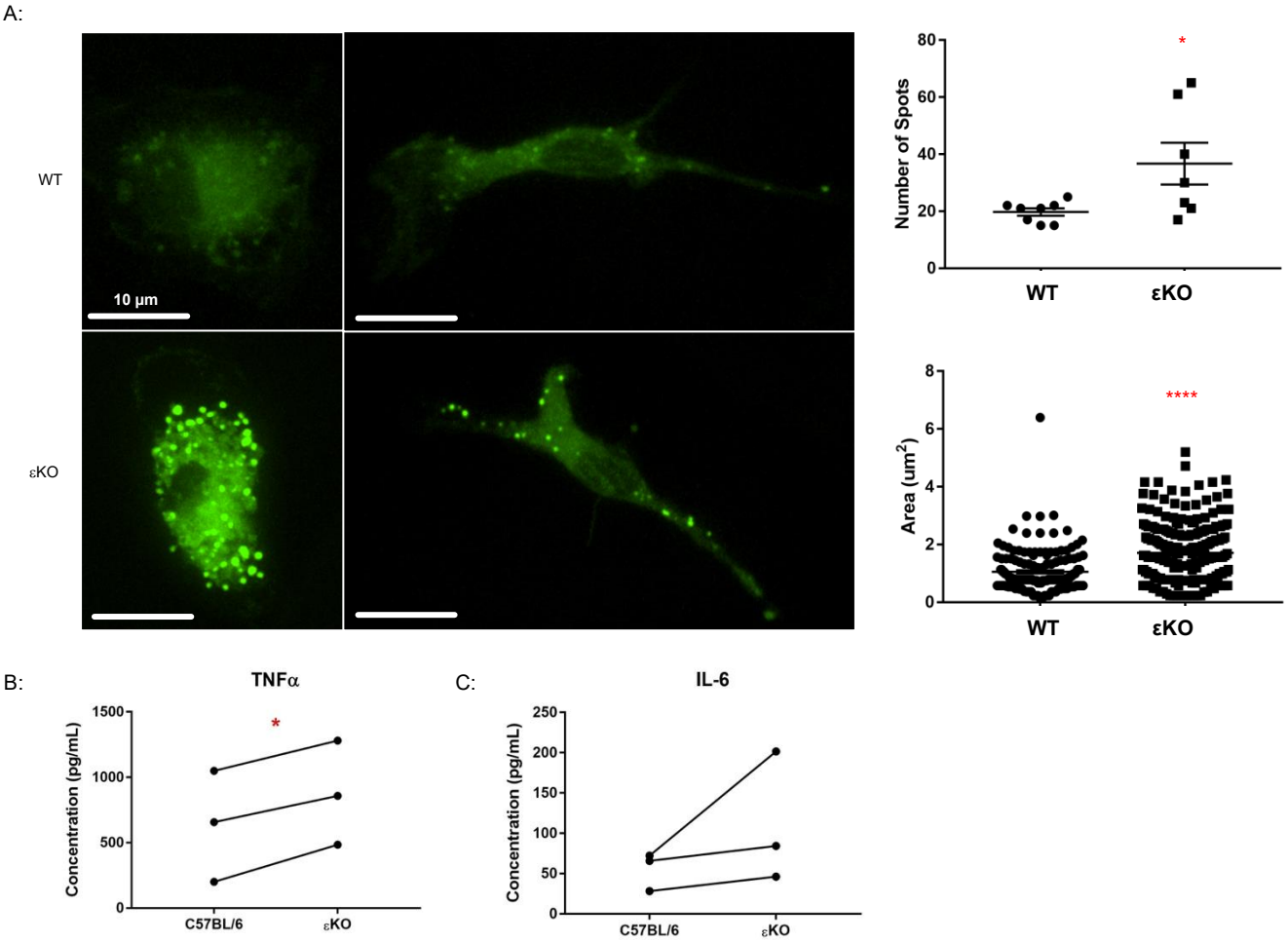

Figure 1: MØ from global PKCε knockout (εKO) mice retain more/larger lipid droplets and release more TNFα. (**A**) C57BL/6 and εKO BMDM were treated with AcLDL (360 µm) for 4h, fixed and lipid droplets stained with BODIPY. Z-stacks were collected, 3-D reconstructions made and number of lipid droplets (each symbol represents one cell) and droplet area (each symbol represents one droplet) was quantified (n = 3). Data are presented as ± SEM. (**B,C**) C57BL/6 and εKO BMDM were incubated with or without immune complexes (2 h). Media was collected and TNFα and IL-6 was quantified by ELISA. Net TNFα and IL-6 release is represented (n = 3). Statistical analysis was preformed by two-tailed unpaired t-test (**A**) and two-tailed paired t-test in (**B,C**). Scale bars: 10 µm. *$p < 0.05$; ****$p < 0.0001$.

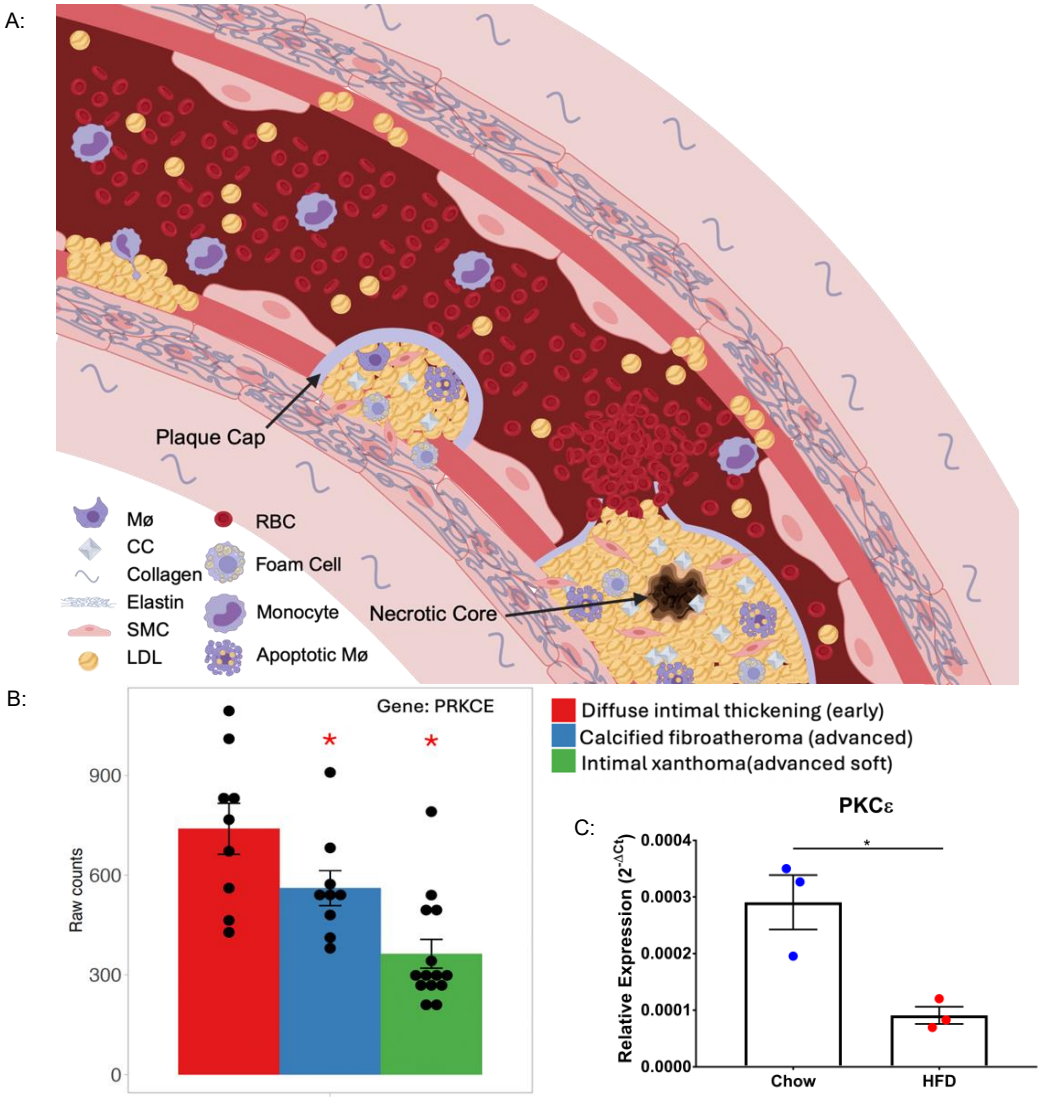

Figure 2: PKCε expression is significantly lower in advanced human plaques and is recapitulated in murine pMACS from hypercholesterolemic mice. (**A**) Schematic of atherogenesis. Created in BioRender. Wells, A. (2024) https://BioRender.com/ b96z554. (**B**) RNAseq of human atherosclerotic plaques (GSE104140) looking at PRKCE raw counts (n = 9-14). (**C**) qPCR of PKCε in elicited pMACs from chow and HFD fed WT mice administered with AAV8-PCSK9 for 4-wks (n=3). Data are presented as ± SEM. Statistical analysis was performed by Limma-voon differential expression analysis (**B**) and two-tailed unpaired t-test (**C**). *$p < 0.05$.

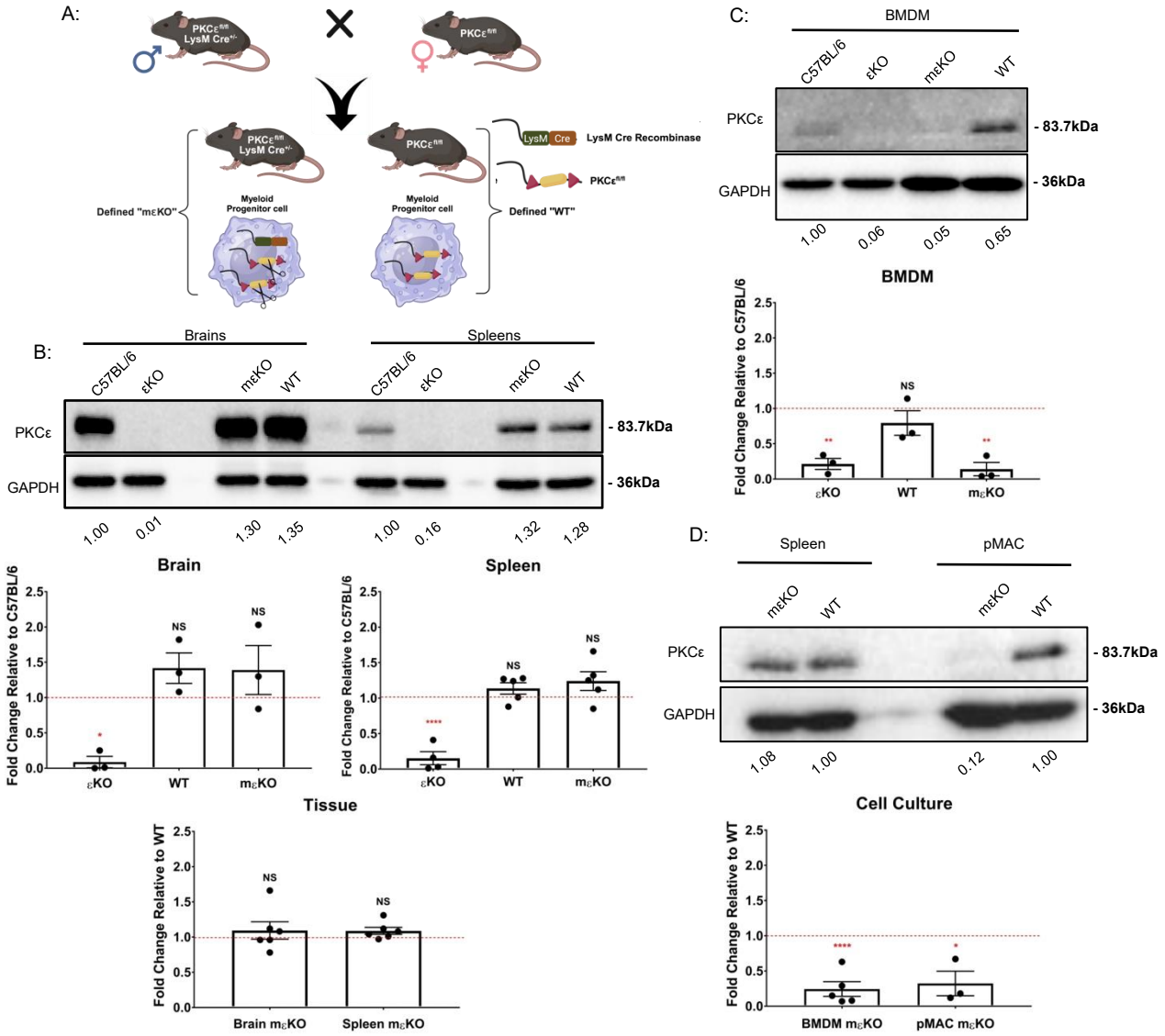

Figure 3: LysM Cre deletes PKCε selectively from myeloid cells. (**A**) Schematic of the LysM Cre PKCε$^{fl/fl}$ breeding strategy. Created in BioRender. Wells, A. (2024) https://BioRender.com/ f22s269. (**B-D**) Western blot and corresponding densitometry probing for PKCε and GAPDH in brains and spleens (**B**), BMDMs, (**C**), and pMACs (**D**) (n=3-6). No substantive reduction in PKCε expression was detected in brain and spleen samples of LysMCre expressers. Little/no PKCε was detected in lysates from BMDMs or pMACs expressing Cre. Data are presented as mean ± SEM. Statistical analysis was performed by two-tailed unpaired t-test (**B-D**) and one-way ANOVA (**B,C**.) Red dotted line indicates respective C57BL/6 or WT that all samples were normalized to. *$p < 0.05$; ***$p < 0.001$; ****$p < 0.0001$.

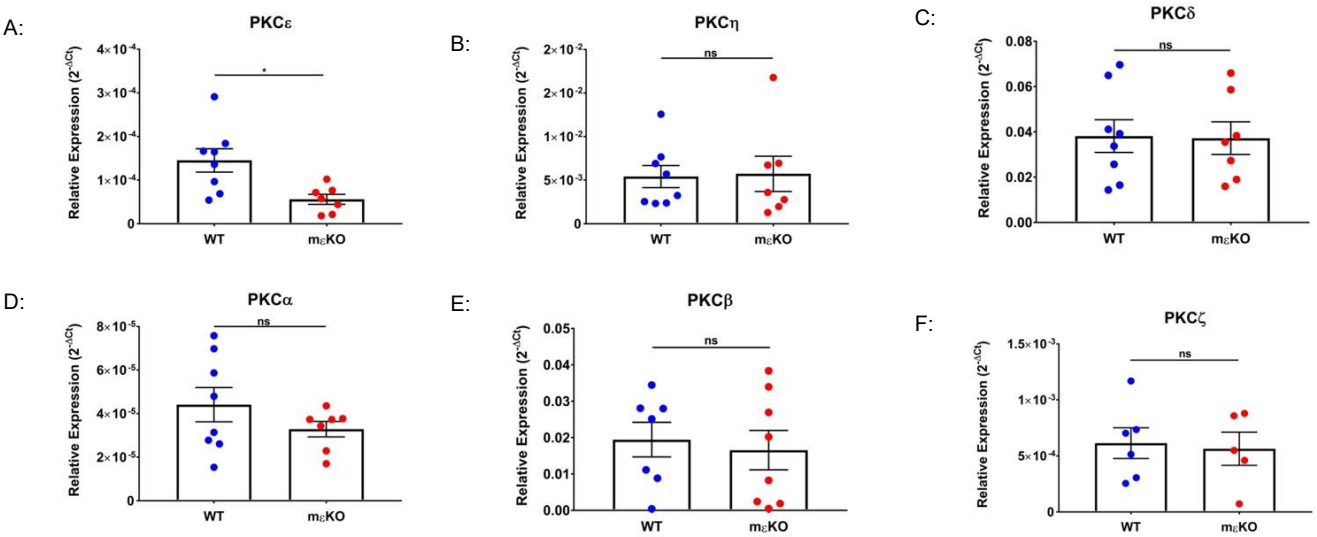

Figure 4: LysM Cre PKCε$^{fl/fl}$ selectively deletes PKCε with no effect on other PKC isoforms. (**A-F**) qPCR for novel (PKCε, PKCΗ, PKCδ), conventional (PKCα, PKCβ), and atypical (PKCζ) PKC isoforms (n = 5-8). Data are presented as mean ± SEM. Statistical analysis was performed by two-tailed unpaired t-test in. *$p < 0.05$.

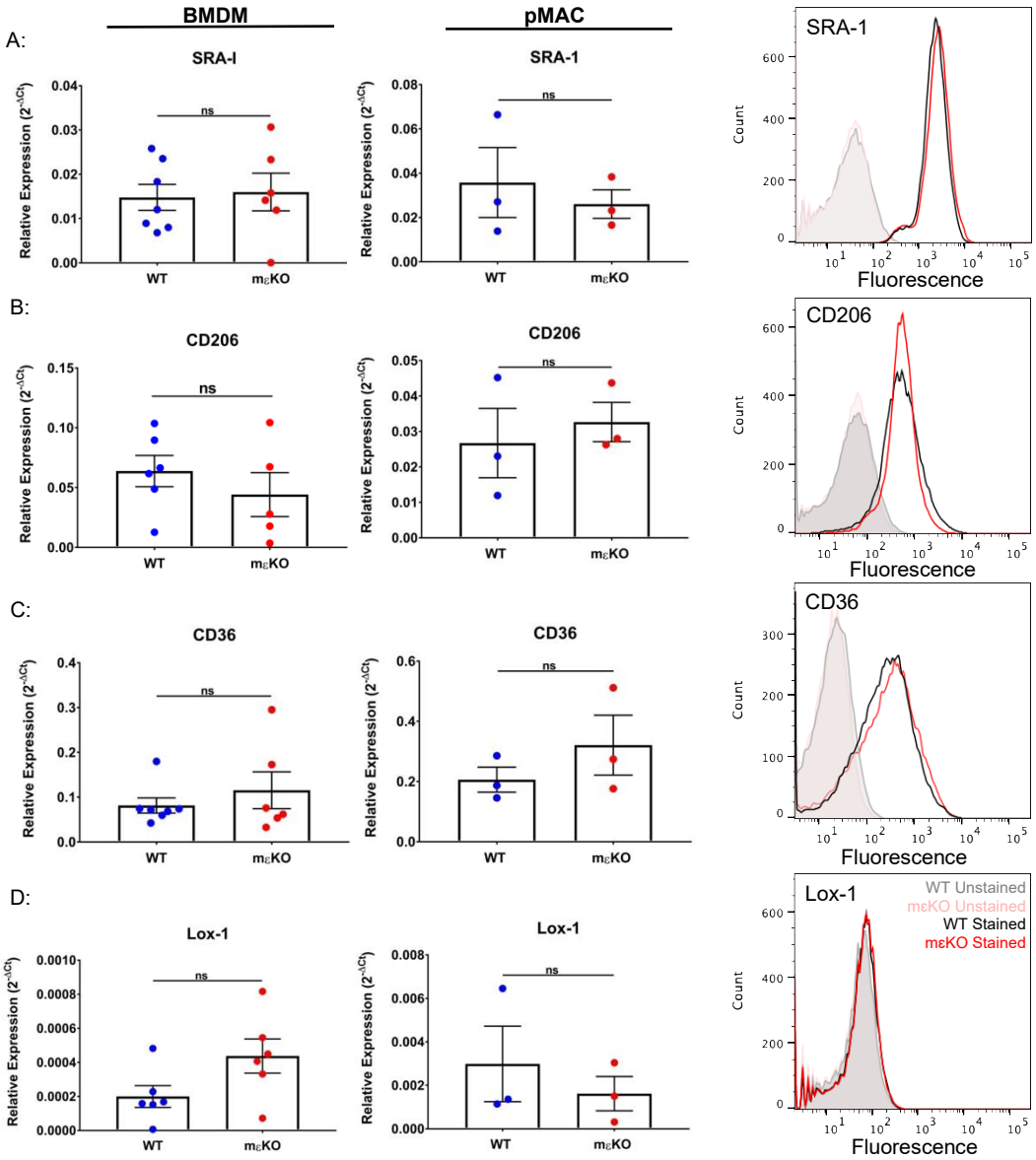

Figure 5: Deletion of PKCε does not affect relative mRNA expression or surface expression of key lipid receptors. (**A-D**) qPCR for SRA-I, CD206, CD36, and Lox-1 in both BMDMs (left) and elicited pMACs (center) (n = 3-6). Flow cytometry of surface expression in BMDM (right) (representative 5 independent experiments). Data are presented as mean ± SEM. Statistical analysis was performed by two-tailed unpaired t-test.

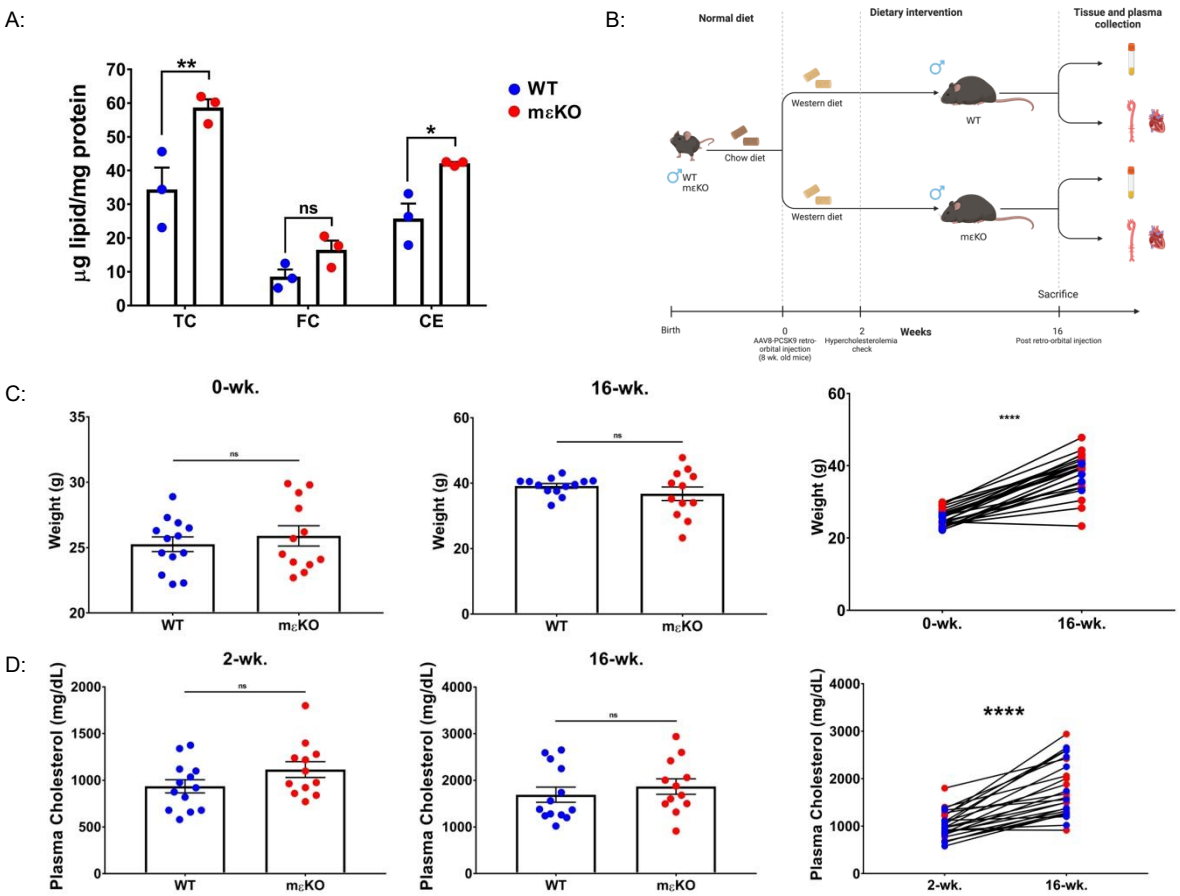

Figure 6: mεKO BMDMs retain more cholesterol in vitro and both WT and mεKO animals have similar weights and degree of hypercholesterolemia in vivo. (**A**) BMDMs were loaded with human Hi-ox-LDL for 24h and assessed for total cholesterol (TC), free cholesterol (FC), and cholesterol esters (CE) (n = 3 with 4 technical replicates per n). (**B**) Timeline of in vivo model. Created in BioRender. Wells, A. (2024) https://BioRender.com/ e98l871. (**C**) Weights were recorded at T = 0 and T = 16 wks. Genotype did not affect weight gain (n = 12-13). (**D**) Blood was collected at 2 and 16 weeks and plasma cholesterol concentration determined. While cholesterol increased over the time course, there was no genotype difference. Each point represents one animal (n =12-13, two independent trials). Data are presented as mean ± SEM. Statistical analysis was performed by one-way ANOVA (**A**), two-tailed paired t-tests (**C,D**) and unpaired t-tests (**C,D**). *$p < 0.05$; **$p < 0.01$; ****$p < 0.0001$.

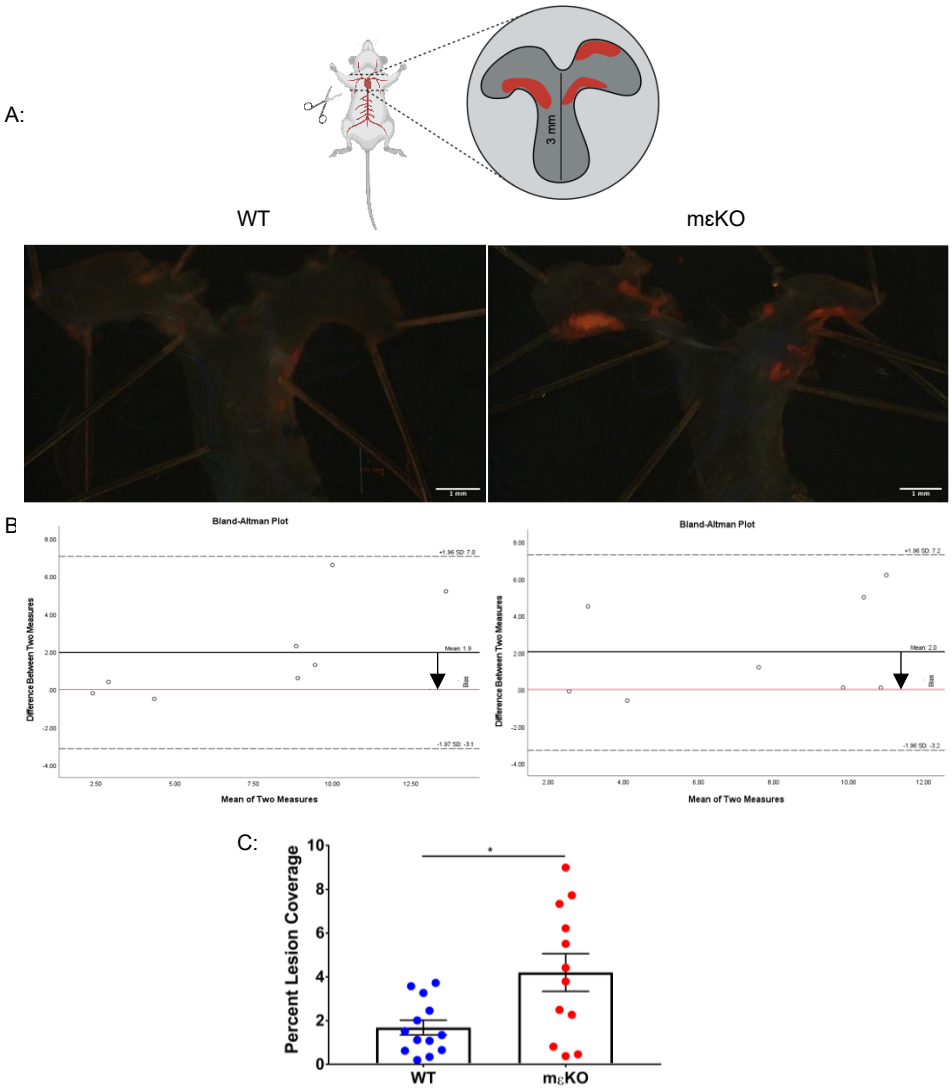

Figure 7: mεKO aortic arches have a higher percent lesion coverage. (**A**) Schematic of the region of descending aorta removed; area analyzed is enlarged. Created in BioRender. Wells, A. (2024) https://BioRender.com/ q65k186. Representative images of Oil red O stained *en face* preparations of T = 16 wk aortic arches. (**B**) A subset of (8) mice were assessed for inter-observer variability, no shift in the bias was detected. (**C**) Quantitation of the aortic arch and 3 mm of descending aorta for percent lesion coverage (n = 12-13, each point represents one animal). Data are presented as mean ± SEM. Statistical analysis was performed by Bland-Altman analysis in (**B**) and two-tailed unpaired t-test in (**C**). Scale Bars: 1 mm. *$p < 0.05$.

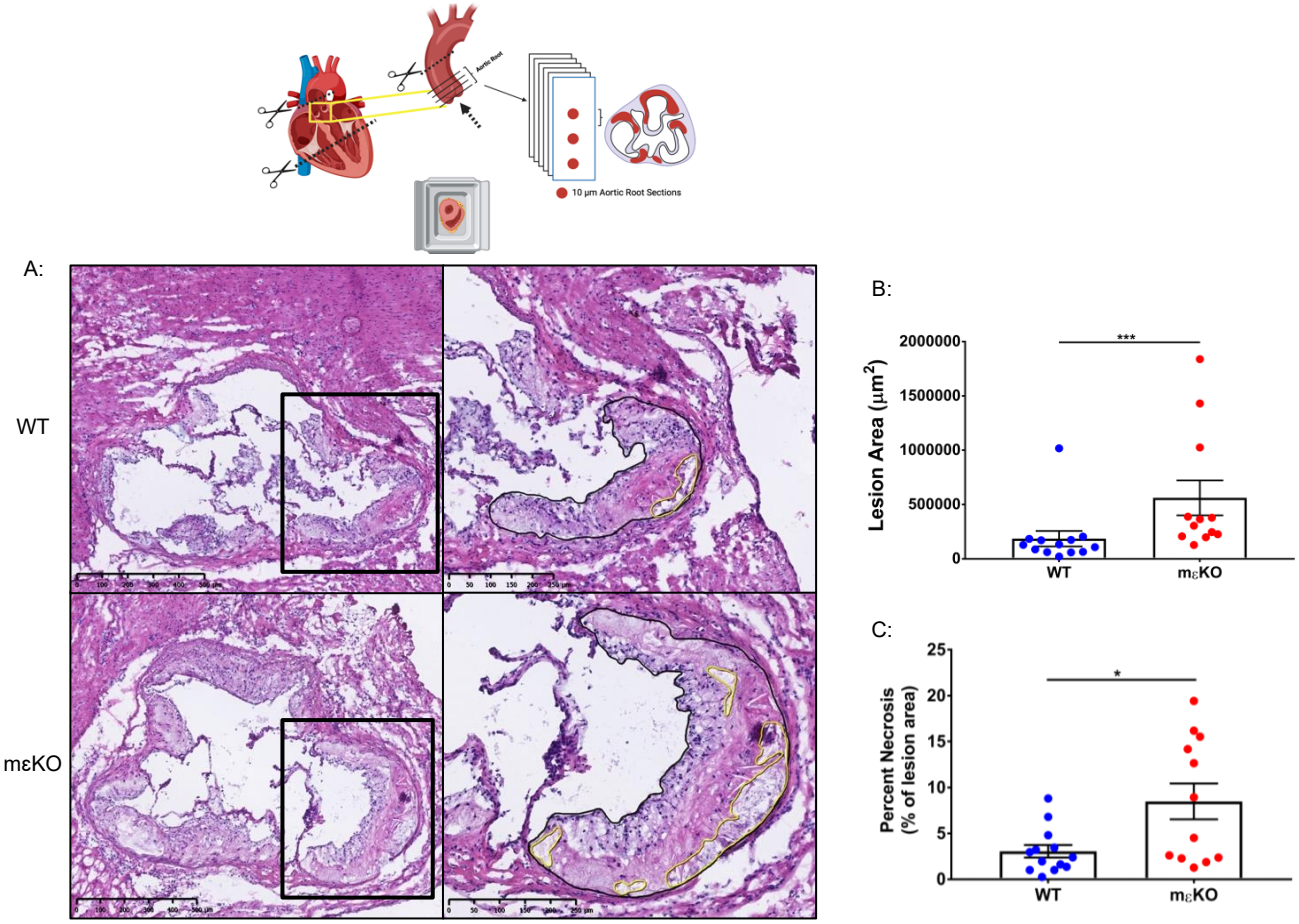

Figure 8: mεKO plaques are larger and more necrotic. (Top) Schematic representation of the location of the aortic root and the cryosectioning strategy. Created in BioRender. Wells, A. (2024) https://BioRender.com/ f19i190. (**A**) Aortic Roots were harvested (T=16 wk), sectioned (10 µm), and stained with H&E. (Right panels): enlarged image of boxed regions. Using the magnified images, plaques were outlined (black lines) and areas of necrosis (yellow outlined) and cholesterol clefts (yellow asterisk) were identified. (**B,C**) The average lesion area and percent necrosis per mouse was calculated (n = 12-13). Each symbol represents one animals. Data are presented as mean ± SEM. Statistical analysis was performed by two-tailed unpaired t-test in B,C. Scale bars: 500 µm (original 5X images) or 250 µm (magnified regions – 10X). *$p < 0.05$; *** $p < 0.001$.

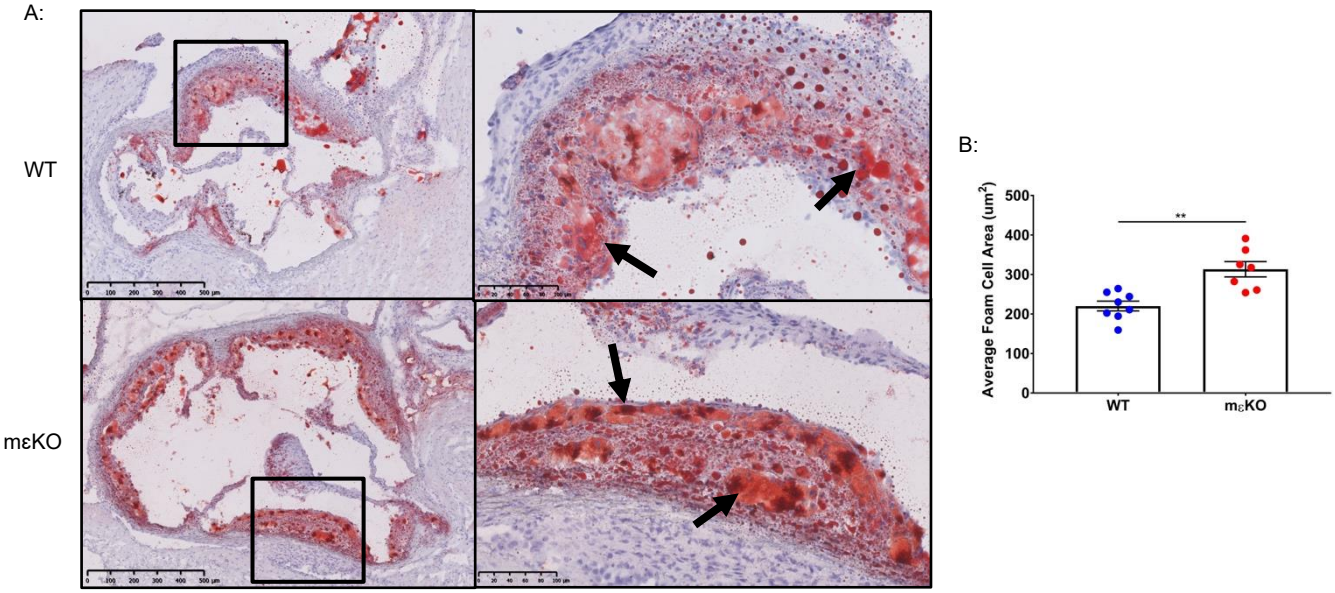

Figure 9: mεKO plaques contain larger foam cells. (**A**) Sildes consecutive to H&E (Figure 9) were stained with ORO to detect lipid. (Right panels): enlarged image of boxed regions. Using the magnified images, foam cells were identified by ORO staining. (**B**) Using the consecutive H&E slides for nuclei determination, the average foam cell area per mouse was calculated (n = 7-8). Data are presented as mean ± SEM. Statistical analysis was performed by two-tailed unpaired t-test. Scale bars: 500 μm (left) or 100 μm (right). $^{**}p < 0.01$.

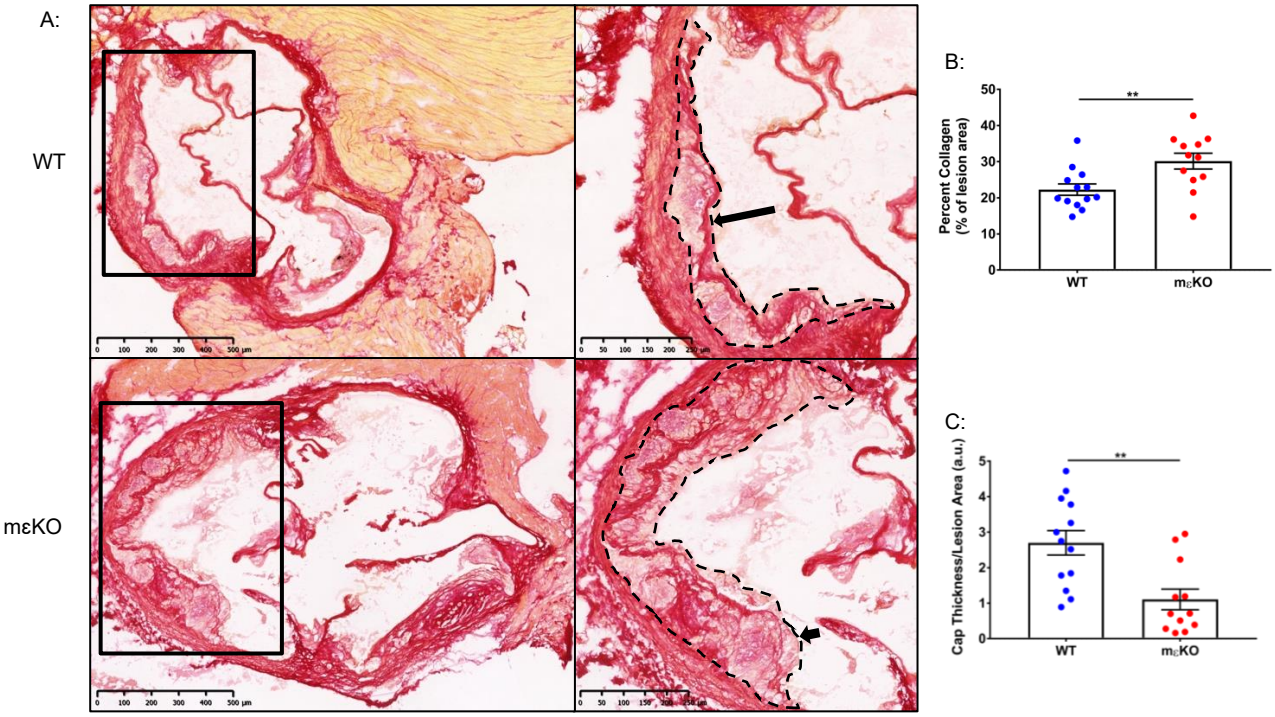

Figure 10: mεKO collagen caps are significantly thinner than WT. (**A**) Plaque sections were stained with with Sirius Red for detection of collagen. (Right panels): enlarged image of boxed regions. Using the magnified images, plaques were outlined (black lines) and total collagen and cap thickness was determined. (**B**) Overall collagen content is reported as a percent of plaque area. (**C**) Collagen overlaying plaques was quantified and reported as thickness normalized to plaque area; arrow identifies the plaque cap; arrowhead denotes a plaque with no cap. (n = 12-13). Data are presented as mean ± SEM. Statistical analysis was performed by two-tailed unpaired t-test. Scale bars: 500 μm (left) or 250 μm (right). $^{**}p < 0.01$.